Invited Review Article: The Josephson bifurcation amplifier

R. Vijay,[1] M. H. Devoret,[2] and I. Siddiqi[1]
[1]*Quantum Nanoelectronics Laboratory, Department of Physics, University of California, Berkeley, California 94720, USA*
[2]*Department of Applied Physics and Department of Physics, Yale University, New Haven, Connecticut 06520-8284, USA*

(Received 28 April 2009; accepted 17 August 2009; published online 17 November 2009)

We review the theory, fabrication, and implementation of the Josephson bifurcation amplifier (JBA). At the core of the JBA is a nonlinear oscillator based on a reactively shunted Josephson junction. A weak input signal to the amplifier couples to the junction critical current I_0 and results in a dispersive shift in the resonator plasma frequency ω_p. This shift is enhanced by biasing the junction with a sufficiently strong microwave current I_{rf} to access the nonlinear regime where ω_p varies with I_{rf}. For a drive frequency ω_d such that $\Omega = 2Q(1-\omega_d/\omega_p) > \sqrt{3}$, the oscillator enters the bistable regime where two nondissipative dynamical states O_L and O_H, which differ in amplitude and phase, can exist. The sharp I_0 dependent transition from O_L to O_H forms the basis for a sensitive digital threshold amplifier. In the vicinity of the bistable regime ($\Omega < \sqrt{3}$), analog amplification of continuous signals is also possible. We present experimental data characterizing amplifier performance and discuss two specific applications—the readout of superconducting qubits (digital mode) and dispersive microwave magnetometry (analog mode). © *2009 American Institute of Physics.* [doi:10.1063/1.3224703]

I. INTRODUCTION

Electrical amplifiers are ubiquitous in experimental physics. They raise the energy of a signal coming from a measurement to a level sufficient to exceed the noise of the recording and processing electronics. Amplifiers are based on nonlinear elements such as the transistor for instance. Typically, such components are dissipative and exhibit a change in their dynamic two terminal resistance in response to an input signal applied to a third terminal, such as a gate. The superconducting tunnel junction[1] is a unique two terminal device that can be operated as either a nonlinear resistor or inductor. A number of different circuit elements, such as a superconducting island or loop, can serve as the third input terminal to couple an external signal, such as an electric charge or magnetic flux, respectively, to the properties of the junction, in particular the critical current I_0. Small variations in I_0 can significantly change the transport properties of the junction under appropriate bias conditions, giving rise to a sensitive amplifier with near quantum limited noise performance.[2–4]

Let us review the basic properties of Josephson tunnel junctions. A Josephson tunnel junction is formed by separating two superconducting electrodes with a barrier such as a thin oxide layer. The current $I(t)$ and voltage $V(t)$ of the junction can be expressed in terms of $\delta(t)$, the gauge-invariant phase difference, as $I(t) = I_0 \sin \delta(t)$ and $V(t) = \varphi_0 d\delta/dt$, where the parameter I_0 is the junction critical current and $\varphi_0 = \hbar/2e$ is the reduced flux quantum. These equations parameterize a nonlinear inductor with inductance $L_J = \varphi_0/\{I_0 \cos(\delta)\}$, which for $\delta \ll 1$ or equivalently $I(t)/I_0 \ll 1$ reduces to $L_{J0} = \varphi_0/I_0$. This inductance is by construction shunted in parallel by the geometric capacitance C_J of the junction, thereby forming an electrical oscillator. The dynamics of this oscillator can be described by the motion of a phase particle with coordinate δ in an anharmonic, sinusoidal potential $U(\delta) = -\varphi_0 I_0 \cos(\delta)$. The natural frequency of small oscillations in this potential, the plasma frequency,[5,6] is $\omega_{p0} = 1/\sqrt{L_{J0}C_J}$. In general, due to the nonlinear nature of the Josephson inductance, the natural frequency of the oscillator will be a function of the oscillation amplitude.

In a Josephson amplifier, an external signal typically modulates the critical current I_0 of the junction, changing both the height of the sinusoidal potential ΔU and the plasma frequency ω_p. Two measurement protocols to detect variations in I_0 are illustrated in Fig. 1. In the dissipative approach (a), the height of the potential barrier $\Delta U(I_0, I_{\mathrm{dc}})$ is determined by biasing the junction with a current $I_{\mathrm{dc}} \lesssim I_0$ and detecting the onset of a finite resistance.[7] In this scheme, the phase particle has sufficient energy to escape the potential well and the phase difference δ advances linearly in time, generating a finite dc voltage. Switching to the finite voltage state of the junction can be avoided by using a dispersive measurement technique to determine $\omega_p(I_0, I_{\mathrm{rf}})$ as shown in Fig. 1(b). This involves applying an alternating current $I_{\mathrm{rf}} \sin(\omega_d t)$ and measuring the time varying voltage across the junction at the drive frequency ω_d.[8–10] If $I_{\mathrm{rf}} \ll I_0$, the junction remains in the superconducting state, and the phase particle oscillates in only one well of the sinusoidal potential with no dc voltage generated. However, the amplitude and phase of the oscillating junction voltage $V(t) = V_J \cos(\omega_d t + \phi_J)$ vary with $\omega_p(I_0, I_{rf})$. The Josephson bifurcation amplifier (JBA) is a dispersive detector that exploits the anharmonicity of the junction oscillator for enhanced measurement sensitivity. In this oscillator, the plasma frequency $\omega_p(I_0, I_{\mathrm{rf}})$

0034-6748/2009/80(11)/111101/17/$25.00

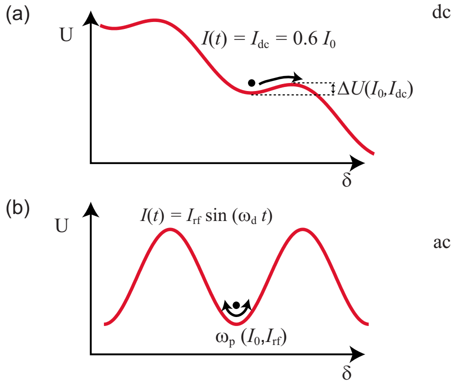

FIG. 1. (Color online) Dissipative (a) and dispersive (b) techniques to determine I_0. In (a), we directly sample the barrier height $\Delta U(I_0, I_{dc})$ by biasing with a current $I(t)=I_{dc}\lesssim I_0$. By measuring the escape rate out of the zero voltage state, one can infer the height of the barrier. In (b), we drive the system with an ac excitation $I(t)=I_{rf}\sin(\omega_d t)$ and measure the response at the drive frequency to determine the plasma frequency $\omega_p(I_0, I_{rf})$.

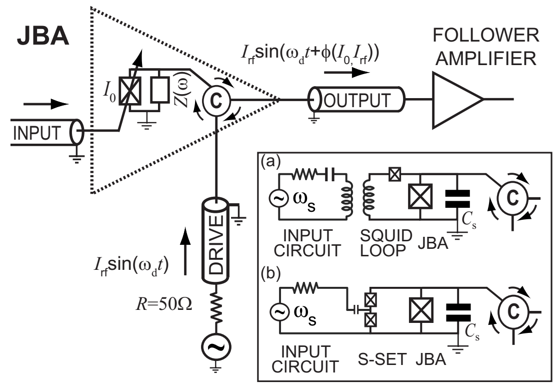

FIG. 3. Schematic diagram of the JBA. A junction with critical current I_0 and a parametrically coupled input is driven by a rf pump signal, which provides the power for amplification. When biased in the vicinity of the dynamical bifurcation point, the phase of the reflected signal ϕ depends sensitively on the input signal. The circulator (C) is used to couple signals in and out of the resonator. It also suppresses the noise of the following amplifier reaching the oscillator and helps ensure that the fluctuations felt by the oscillator correspond to the noise of a 50 Ω resistor at the bath temperature T. Inset: examples of parametric input coupling circuits using a SQUID and S-SET.

varies not only with the critical current I_0 but also with the drive amplitude I_{rf}. When biased with a sufficiently strong current I_{rf}, the plasma frequency shift for a small modulation in I_0 is significantly increased[9,11] as compared to the case with lower drive current when the oscillator is in the linear regime.

The dependence of the plasma frequency on drive amplitude is depicted in Fig. 2 where the steady state amplitude V_J and the phase ϕ_J of the junction voltage are plotted as a function of ω_d and I_{rf} (see Sec. II for theory). The resonant response sharpens and shifts to lower frequency as the drive amplitude is increased. At higher drive powers, the system bifurcates from a single valued to a bistable regime. When the drive frequency ω_d (solid vertical line) is sufficiently detuned from the small oscillation plasma frequency ω_{p0}, the system can have two possible oscillation states (O_L and O_H),

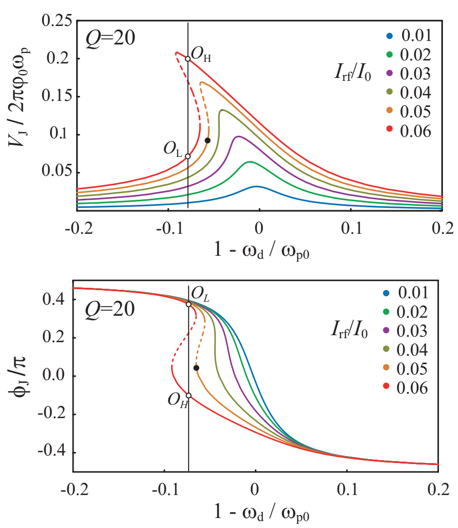

FIG. 2. (Color) Computed steady state junction (a) voltage amplitude V_J and (b) phase ϕ_J of the JBA when driven with an ac excitation $I(t) = I_{rf}\sin(\omega_d t)$. The different traces correspond to different drive amplitudes I_{rf}. Solutions are plotted as a function of normalized drive frequency for an oscillator with $Q=20$. O_L and O_H denote the low amplitude phase lagging and the high amplitude phase leading oscillation states, respectively. The black dot indicates a typical bias point where the system is highly sensitive to changes in I_0.

which differ in amplitude and phase. The dashed lines on the response curves indicate unstable solutions. For a bias point such as the one indicated by the black dot in the figure, a small decrease in I_0 will cause the oscillator to evolve from O_L to O_H, thus realizing a sensitive threshold detector for I_0. The smallest variation in I_0 that can be resolved is limited by thermal or quantum fluctuations, which broaden this transition. In this digital mode of operation, small changes in the critical current translate into changes in the occupation probability of the two dynamical states.

The circuit schematic of the JBA is shown in Fig. 3. The tunnel junction is shunted in parallel by an additional purely reactive impedance $Z(\omega)$, which in the simplest case is a capacitor with $C_S \gg C_J$. This reactive impedance allows one to tune the resonant frequency and the quality factor of the resonator. The junction can also be embedded in a transmission line cavity to form a nonlinear transmission line resonator.[12,13] We will consider the capacitively shunted case in detail in this review though a brief description of the transmission line version will be provided in Sec. II. The input signal couples to the junction I_0. Examples of input circuits used to couple weak electrical signals are shown in the inset. In (a), an external signal is inductively coupled to a superconducting quantum interference device (SQUID) loop, which modulates I_0. In (b), a superconducting single electron transistor (S-SET) is used to couple signals capacitively. A microwave generator with $Z_0=50\ \Omega$ output impedance drives a current $I_{rf}(t)\sin(\omega_d t)$ via the circulator (C), which allows microwave signals to flow in one direction. The signal reflected from the resonator is the amplifier output and is coupled to a cryogenic semiconductor amplifier through the adjacent port of the circulator. This signal is further amplified and demodulated at room temperature using quadrature mixers to determine the signal amplitude and phase.

The idea of amplifying signals using a bifurcation is quite common and observed in electrical, optical, chemical, and biological systems (see Ref. 14 and references therein).

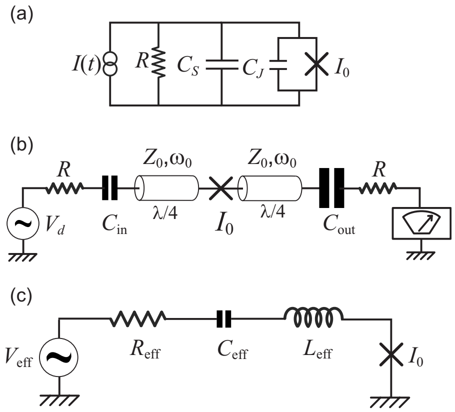

FIG. 4. (a) Circuit diagram of the JBA. (b) Circuit diagram of the CBA with a half-wave transmission line cavity embedded with a Josephson junction in the middle. (c) The equivalent LCR circuit for the CBA.

Recently, such nonlinear behavior has been observed in nanomechanical resonators and is being extensively studied for applications in parametric sensing.[15] A biological example of bifurcation amplification in nature is the human ear. The cochlea in our ear is biased close to a Hopf bifurcation,[16] which leads to several remarkable properties in our hearing such as compression of dynamic range, infinitely sharp tuning at zero input, and generation of combination tones. The ear is essentially a nonlinear amplifier, i.e., the response depends quite strongly on the strength of the input signal. Researchers in robotics and medical sciences are currently in the process of constructing a hearing sensor, which can mimic the nonlinear properties of the cochlea.[17] In superconducting devices, the Josephson parametric amplifier[18] also exploits proximity to a bifurcation. These devices are capable of achieving large gain with near quantum limited noise and can show quantum effects such as squeezing of noise below the standard quantum limit.[19] Note that the JBA can also be operated as a conventional parametric amplifier by combining a weak input signal along with the drive signal. When biased in the vicinity of the bifurcation points, the system can exhibit parametric gain[20] like in recently developed amplifiers based on multi-junction (rather than single junction) circuits embedded in microwave cavities[21,22]

In this review, we will detail the theory of operation of the JBA in Sec. II, focusing in particular on the case where the shunting impedance $Z(\omega)$ is a simple capacitor. In Sec. III, we discuss device design and fabrication. The cryogenic measurement setup is detailed in Sec. IV. In Sec. V, measurements characterizing the stand alone amplifier are presented. In Sec. VI, we discuss two particular applications of the JBA—measurements of the quantronium qubit and high speed magnetometry. We present concluding remarks in Sec. VII.

II. THEORY

We study bifurcation amplification in two types of circuits. The first one is a lumped element resonator where we shunt the Josephson junction with a capacitor to form the nonlinear resonator. This circuit is shown in Fig. 4(a). Here, I_0 is the critical current of the junction, C_J is the intrinsic junction capacitance, $C_S \gg C_J$ is the shunt capacitance to tune the resonant frequency, and R is the real part of the current source impedance, which provides damping. In the second technique, we embed a Josephson junction in a half-wave transmission line resonator as shown in Fig. 4(b). If we make a single mode approximation for the transmission line resonator near its resonant frequency, one arrives at the equivalent LCR circuit shown in Fig. 4(c). The values of the effective circuit elements are given by the following equations

$$V_{\text{eff}} = Z_0 \omega_0 C_{\text{in}} V_d, \quad R_{\text{eff}} = Z_0^2 R \omega_0^2 C_{\text{out}}^2, \tag{1}$$

$$L_{\text{eff}} = \pi Z_0 / 2\omega_0, \quad C_{\text{eff}} = 2/(\pi Z_0 \omega_0),$$

where Z_0 is the characteristic impedance of the transmission line, $C_{\text{in}} \ll C_{\text{out}}$ are the input and output coupling capacitors, ω_0 is the bare resonant frequency of the cavity set by its length and speed of microwaves in the transmission line and $R=50\ \Omega$ as before is the characteristic impedance of the microwave feed lines. The transmission line version, which has been dubbed the cavity bifurcation amplifier (CBA), essentially works on the same principle as the lumped element JBA though it offers some practical advantages such as ease of fabrication, absence of dielectric layers, possibility of multiplexing, etc. In this section, we will begin by establishing the connection between the JBA and the CBA, but we will restrict the detailed description to that of the JBA. For more details on the CBA, see Ref. 23.

The classical differential equations describing the dynamics of a Josephson junction oscillator driven with a rf current for the circuits depicted in Figs. 4(a) and 4(c) are given below,

$$C_S \varphi_0 \frac{d^2\delta(t)}{dt^2} + \frac{\varphi_0}{R}\frac{d\delta(t)}{dt} + I_0 \sin[\delta(t)] = I_{\text{rf}} \cos(\omega_d t) + I_N(t), \tag{2}$$

$$\left(L_{\text{eff}} + \frac{\varphi_0}{I_0\sqrt{1-\dot{q}^2/I_0^2}}\right)\frac{d^2 q(t)}{dt^2} + R_{\text{eff}}\frac{dq(t)}{dt} + \frac{q}{C_{\text{eff}}} = V_{\text{rf}}\cos(\omega_d t) + V_N(t). \tag{3}$$

In Eq. (2), δ is the gauge-invariant phase difference across the junction, ω_d is the drive frequency, and $\varphi_0 = \hbar/2e$ is the reduced flux quantum. The noise current $I_N(t)$ models the thermal noise of the source impedance R. In Eq. (3), q is the charge on the capacitor C_{eff} and $V_N(t)$ is the effective thermal noise of the impedance R_{eff}. Under appropriate driving conditions, this nonlinear oscillator can have two steady driven states differing in amplitude and phase.[9,24] Even though Eqs. (2) and (3) look different, especially with respect to the location of the nonlinear term, they reduce to the same effective equation. If we assume harmonic solutions for $\delta(t)$ or $q(t)$ at the drive frequency ω_d of the form $y(t)e^{i\omega_d t}$+c.c., we can show that the equation of motion for the dimensionless slowly varying complex amplitude $u(\tau)$ corresponding to Eqs. (2) and (3) can be reduced to

$$\frac{du}{d\tau} = -\frac{u}{\Omega} - iu(|u|^2 - 1) - i\sqrt{\beta} + f_N(\tau), \tag{4}$$

where

TABLE I. Variables used in Eqs. (2)–(4) expressed in terms of circuit parameters.

Parameter	JBA	CBA
ω_{p0}	$\sqrt{\frac{I_0}{\varphi_0 C_s}}$	$\sqrt{\frac{1}{(L_{\mathrm{eff}}+\varphi_0/I_0)C_{\mathrm{eff}}}}$
Q	$RC_s\omega_{p0}$	$\frac{\pi Z_0}{2R_{\mathrm{eff}}}$
u	$\sqrt{\frac{\omega_{p0}^2}{4\omega_d(\omega_{p0}-\omega_d)}}y$	$\sqrt{\frac{1}{2\Omega\varepsilon^2}}\frac{\omega_d}{I_0}y$
β	$\frac{\omega_{p0}^6 I_{\mathrm{rf}}^2}{64 I_0^2\omega_d^3(\omega_{p0}-\omega_d)^3}$	$\frac{V_{\mathrm{rf}}^2}{\varphi_0^2\omega_d^2}\left(\frac{1}{2\Omega\varepsilon^2}\right)^3$

$$\Omega = 2Q(1-\omega_d/\omega_{p0}) \tag{5}$$

is the reduced drive detuning, ω_{p0} is the resonant frequency for small oscillations, Q is the quality factor, $\tau=(\omega_{p0}-\omega_d)t$ is the dimensionless slow time, β is the reduced drive power, and $f_N(\tau)$ is the reduced noise term. Equation (4) has been derived under the rotating wave approximation with only leading order nonlinear terms being retained in Eqs. (2) and (3). The expressions for ω_{p0}, Q, u, and β for the JBA and the CBA are given in Table I, where $\varepsilon=\sqrt{(1+L_{\mathrm{eff}}I_0/\varphi_0)/Q}$. So apart from different expressions for the reduced variables in the terms of circuit parameters, the nonlinear dynamics of JBA and CBA oscillators converges to the universal form Eq. (4) for large Q. Hence, from now on, we will restrict our discussion to the JBA.

The scaled steady state solutions of Eq. (4) $(du/d\tau=0)$ for the JBA are plotted in Fig. 2 for different excitation amplitude I_{rf}. These curves are computed with the noise term $f_N(\tau)$ set to zero. The different curves correspond to different drive strength. For $I_{\mathrm{rf}} \ll I_0$, the response is linear with a characteristic Lorentzian line shape. In this regime, the phase particle only samples small values of δ so that the sinusoidal potential is well approximated by a parabola, which describes harmonic behavior. For increasing drive amplitude, the higher order nonlinear terms contribute and reduce the plasma frequency $\omega_p(I_0,I_{\mathrm{rf}})$, but the response is still single valued. For sufficiently strong drive, the oscillator bifurcates and can occupy one of two metastable states (O_L and O_H). These states differ significantly in oscillation amplitude and phase. The dashed lines in Fig. 2 indicate the unstable solutions.

To illustrate how a small variation in critical current can be detected, the phase response of the oscillator for two different values of I_0 is plotted in Fig. 5 for three different drive currents corresponding to the linear response regime, the single-valued nonlinear regime, and the bifurcation regime described above. An input signal modulates the critical current and shifts the plasma frequency, shown in Fig. 5 as a displacement of the response curves. To operate the JBA, a drive current at fixed frequency ω_d is applied. An alternative technique where the drive amplitude is kept fixed but the frequency is swept has been recently presented in Ref. 25. A shift in ω_p is detected as a shift in phase of the reflected

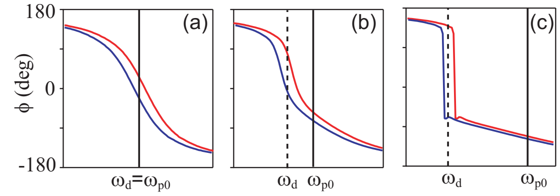

FIG. 5. (Color) Principle of operation of the JBA. The curves in all three panels are the reflected signal phase response for three different drive powers. The red (right) and blue (left) curves correspond to two different values of the small oscillation plasma frequency ω_{p0}. The value of ω_{p0} for the blue curve is indicated by the vertical solid line. Panel (a) is for the smallest drive power and corresponds to linear regime. For a larger drive power in (b), the JBA oscillator is in the single-valued nonlinear regime. When biased with sufficient power to access the bistable regime (c), the phase response exhibits a sharp transition. Thus, the maximum phase shift for a given change in ω_{p0} increases with drive power [(a)–(c)] and is achieved at the bias points with increasing detuning as indicated by the vertical dashed lines.

signal output, as described in Fig. 3. In the linear regime shown in Fig. 5(a), the maximum phase shift and thus the maximum gain are achieved by driving the oscillator at $\omega_d=\omega_{p0}$ as indicated by the solid line. Sensitivity can be improved by increasing the quality factor $Q=RC_s\omega_{p0}$ of the oscillator but at the direct cost of reducing the amplifier bandwidth. Another approach to improve sensitivity, which is at the heart of the JBA, is to increase the drive current to access the nonlinear regimes shown in Figs. 5(b) and 5(c). In Fig. 5(b), the phase response is sharper on the lower frequency part of the response curve, and a greater sensitivity can be obtained by driving at a frequency ω_d red detuned from ω_{p0}, as indicated by the dashed line. For yet stronger drives, the response curve transitions sharply between the two branches, as shown in Fig. 5(c). If the drive frequency ω_d is chosen in the vicinity of this bifurcation point, then the oscillator will occupy one oscillation state or the other depending on the value of I_0. By adjusting the drive current amplitude and frequency, the phase difference in the reflected signal between these states can approach 180°, realizing a very sensitive threshold detector for small variations in I_0, which does not rely on switching to the dissipative finite voltage state.

In the linear and the single-valued nonlinear regime, the minimum critical current variation that can be resolved and thus the ultimate sensitivity of the amplifier depend on the smallest phase or amplitude shift, analog quantities, that can be resolved by the cryogenic microwave measurement electronics in a given time interval.[26,27] In the bifurcation regime, the reflected signal phase is a digital quantity with a sufficiently large difference between the two oscillation states that it can be fully resolved within practical integration times ($\sim$100 ns). The amplifier sensitivity in the bifurcation regime is thus set by the minimal critical current variation, which causes the oscillator to switch from one dynamical state to the other. This is determined by the dominant fluctuations, thermal or quantum, in the system. Sensitivity is thus not limited by microwave electronics, an important practical advantage.

For a given drive frequency ω_d such that $\Omega=2RC_S(\omega_{p0}-\omega_d)>\sqrt{3}$, the systems exhibits bistability within a certain range of drive amplitude such that $I_B^-<I_{\mathrm{rf}}<I_B^+$. Here I_B^- and

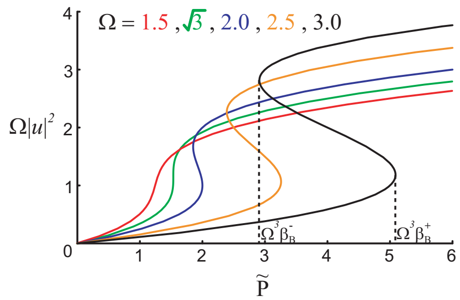

FIG. 6. (Color) Steady state solutions of Eq. (4) for increasing (left to right) values of reduced detuning Ω. The magnitude squared of reduced oscillation amplitude is plotted as a function of reduced drive power $\tilde{P}=\Omega^3\beta$. The x and y axes have been scaled to clearly depict the variation with Ω. We observe multivalued solutions for $\Omega>\sqrt{3}$. The turning points of the curves for $\Omega>\sqrt{3}$ are the bifurcation points ($\beta_B^{\pm}$) and are indicated for the curve with $\Omega=3.0$.

I_B^+ are called the lower and upper bifurcation currents, respectively. Figure 6 shows a plot of the steady state solutions of Eq. (4) as a function of reduced drive power for different values of reduced drive detuning. Multivalued solutions exist only for $\Omega>\sqrt{3}$. The bifurcation points are the turning points of these curves where the slope $d|u|^2/d\beta=\infty$. The reduced bifurcation points are indicated $[\beta_B^{\pm}\propto(I_B^{\pm})^2]$ for the curve with $\Omega=3.0$. The saddle-node bifurcation is found in the vicinity of the upper bifurcation current I_B^+, which is given by

$$I_B^+ = \frac{16}{3\sqrt{3}} I_0 \alpha^{3/2}\left(1+\frac{9}{16Q^2\alpha^2}\right)^{1/2}, \tag{6}$$

where $\alpha=1-\omega_d/\omega_{p0}$ is the dimensionless detuning of the drive. The above formula has been computed by retaining only one nonlinear term in the expansion of $\sin(\delta)$ using the method outlined in Ref. 24 and is given here in the limit of high quality factor Q ($\gtrsim 10$) such that $\Omega=2Q\alpha\gg 1$. The JBA, when operated as a digital threshold detector, is biased near this point by ramping the current. Hence, in what follows, whenever we mention bifurcation point/current, we mean the upper bifurcation point/current.

There are two important quantities that go into determining the sensitivity of the JBA to changes in critical current when operated as a digital threshold detector. The first quantity is the shift in the bifurcation current I_B^+ with critical current I_0. This quantity can be written as follows:

$$\frac{\partial I_B^+}{\partial I_0} = \frac{I_B^+}{I_0}\frac{3}{4\alpha}. \tag{7}$$

We can infer from the above equation that the fractional variation in the bifurcation current ($\partial I_B^+/I_B^+$) is always larger than the fractional variation in critical current ($\partial I_0/I_0$) since $3/4\alpha>1$. The second quantity that determines the sensitivity of the JBA is the intensity of fluctuations at a given temperature T. These fluctuations induce switching between the metastable states of the JBA, which gives a finite width to the transition from the low (O_L) to the high (O_H) amplitude state. In the classical regime ($k_BT\gg\hbar\omega_{p0}$), this dynamical switching can be described by an Arrhenius law in which the rate of escape from an effective cubic metapotential

$$\Gamma_{\rm esc}^{\rm rf} = (\omega_a/2\pi)\exp(-\Delta U_{\rm esc}^{\rm rf}/k_BT) \tag{8}$$

is written as the product of an attempt frequency $\omega_a/2\pi$ and a Boltzmann factor, which contains the barrier height $\Delta U_{\rm esc}^{\rm rf}$, and the system temperature T. In this case, the effective barrier height[24] is

$$\Delta U_{\rm esc}^{\rm rf} = U_{\rm esc}^{\rm rf}[1-(I_{\rm rf}/I_B)^2]^{3/2}, \tag{9a}$$

$$U_{\rm esc}^{\rm rf} = \frac{64}{9\sqrt{3}}\varphi_0 I_0 \alpha, \tag{9b}$$

where the coefficient $U_{\rm esc}^{\rm rf}$ is given to lowest order in $1/(\alpha Q)$. Similarly, the attempt frequency in the metapotential is given by

$$\omega_a = \omega_{a0}[1-(I_{\rm rf}/I_B)^2]^{1/2}, \tag{10a}$$

$$\omega_{a0} = 4Q\omega_p\alpha^2/(3\sqrt{3}), \tag{10b}$$

where we have assumed that the JBA is biased sufficiently close to the bifurcation point resulting in an overdamped motion in the rotating frame. We should point out that for bias points sufficiently far from the bifurcation point, the motion in the rotating frame is underdamped and Eq. (10a) has a different power law[28] but Eq. (9a) remains valid.

We now introduce the idea of a switching probability curve or an "S-curve." If the JBA is biased by ramping the current $I_{\rm rf}$ to a value slightly lower than I_B^+, there is a finite probability that it will make a transition from the low amplitude state to the high amplitude state in a given time t_w. This is called the switching probability $P_{\rm switch}$ at that bias point. Since we know the escape rate $\Gamma_{\rm esc}^{\rm rf}$ from the low amplitude state to the high amplitude state of the JBA, we can define the probability of switching in a given time t_w,

$$P_{\rm switch}(I_{\rm rf},I_0,t_w) = 1-\exp[-t_w\Gamma_{\rm esc}^{\rm rf}(I_{\rm rf},I_0)], \tag{11}$$

where $P_{\rm switch}(I_{\rm rf},I_0)$ has been defined as function of two parameters—the drive amplitude $I_{\rm rf}$ and the critical current I_0—as we are interested in the variation in $P_{\rm switch}$ with respect to these two parameters. The S-curve is essentially the plot of $P_{\rm switch}$ versus $I_{\rm rf}$ for a given I_0 and varies smoothly from zero to one (Fig. 7). The finite width of this S-curve is set by the intensity of fluctuations and hence the temperature. Clearly, a change in the value of critical current will shift the S-curve, resulting in a change in $P_{\rm switch}$. This is the principle of detection in the digital mode. The switching probability is measured by sending many pulses to the JBA and recording the resulting oscillation state of the JBA for each pulse. The shift in S-curves is essentially related to the shift in the bifurcation current and can be inferred from Eq. (7),

$$\Delta I_{\rm shift} = \frac{\partial I_B^+}{\partial I_0}\Delta I_0 = \frac{I_B^+}{I_0}\frac{3}{4\alpha}\Delta I_0. \tag{12}$$

The computation of the S-curve width is subtle. Since Eq. (8) (and hence Eq. (11)) is only valid for small escape rates ($\Delta U_{\rm esc}^{\rm rf}\gtrsim k_BT$), it essentially breaks down near the top of the S-curve where the switching rates are very high. So we compute the width of the S-curve in terms of the drive amplitude using a different procedure. The upper boundary of the S-curve is clearly set by I_B^+ since the escape barrier vanishes at the bifurcation point. For the lower boundary we use the

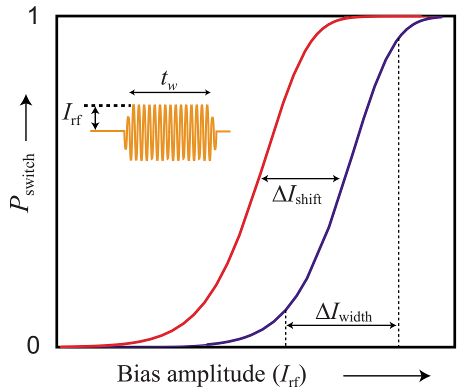

FIG. 7. (Color online) Switching probability P_{switch} of the JBA when energized with a pulse of duration t_w and amplitude I_{rf}. The curves indicate the probability of switching, as a function of I_{rf} from the low amplitude to the high amplitude state when biased near the upper bifurcation point (I_B^+). The red (left) and blue (right) curves correspond to smaller and larger junction critical currents, respectively. The shift (ΔI_{shift}) depends on the change in I_0 and the relative detuning α. The width (ΔI_{width}) depends on the intensity of fluctuations in the oscillator.

point when $\Delta U_{\text{esc}}^{\text{rf}} \sim k_B T$ since P_{switch} starts becoming nonzero around that point. The resulting width is given by

$$\Delta I_{\text{width}} = I_B^+ \left(\frac{k_B T}{U_{\text{esc}}^{\text{rf}}} \right)^{2/3}, \tag{13}$$

where $U_{\text{esc}}^{\text{rf}}$ is given by Eq. (9b). Note that this definition of ΔI_{width} is not strictly identical to that depicted in Fig. 7 where we qualitatively illustrate the idea of the width of an *S*-curve. We get a unit change in P_{switch} when the shift in the *S*-curve is about the same as its width. Combining the above two equations, we can compute the change (ΔI_0) in critical current that can be resolved in a single pulsed measurement or the critical current resolution as

$$\Delta I_0 = \frac{3^{2/3}}{4} I_0^{1/3} \left(\frac{k_B T}{\varphi_0} \right)^{2/3} \alpha^{1/3} (1-\alpha)^{-2}. \tag{14}$$

We note that the critical current resolution depends quite weakly on most parameters, the strongest being the temperature ($T^{2/3}$). The dependence on I_0 is quite weak ($I_0^{1/3}$), which means that there is flexibility in choosing the value of junction critical current. If the total time taken for one pulsed measurement is t_{pulse} (set by Q and noise temperature of the microwave amplification chain), then we can express the critical current resolution ΔI_0 in terms of a critical current sensitivity per unit bandwidth as

$$S_{I_0}^{1/2} = \frac{3^{2/3}}{4} I_0^{1/3} \left(\frac{k_B T}{\varphi_0} \right)^{2/3} \alpha^{1/3} (1-\alpha)^{-2} \sqrt{t_{\text{pulse}}}. \tag{15}$$

An important point to be noted is that the above analysis has been done in the limit of large Q and small escape rates $\Gamma_{\text{esc}}^{\text{rf}}$ in order to simplify calculations and see trends clearly. Often, many of these approximations become too crude in real experiments, especially for small $Q<20$, and the only way to obtain accurate predictions is with full numerical simulations of Eq. (2). Nevertheless, the above formulae serve as a guide to the phenomena and provide quick estimates. For more details on the calculation, see Ref. 20. Furthermore, we have neglected intrinsic fluctuations in the junction critical current as these have a well studied intensity and $1/f$ frequency spectrum[29] which diminishes their contribution at microwave frequencies.

In the quantum regime $k_B T \ll \hbar\omega_{p0}$, the above analysis remains valid if we replace T with an effective temperature $T_{\text{eff}} = \hbar\omega_d / 2k_B$. This result has been predicted theoretically using the idea of quasienergies in the rotating frame for both underdamped[30,31] and overdamped motion in the rotating frame.[32] Note that this effective temperature is different from the saturation temperature seen in the escape to the voltage state in a dc current-biased junction ($T^* = \hbar\omega_d / 7.2 k_B$), which is determined by a tunneling rate at low temperatures.[33] One can also arrive at these results by treating the JBA as a parametric amplifier when biased near the bifurcation point. The parametric amplification process converts the virtual zero point quantum fluctuations into real classical fluctuations. The effective temperature of this classical bath tends to $T_{\text{eff}} = \hbar\omega_d / 2k_B$ as the bath temperature $T \to 0$. For operating points close to the bifurcation point, one can compute the full expression for the effective temperature[34] as

$$T_{\text{eff}} = \frac{\hbar\omega_d}{2k_B} \coth\left(\frac{\hbar\omega_d}{2k_B T} \right), \tag{16}$$

and we note that this expression tends to the correct limits as $T \to 0, \infty$. This expression is identical to the one obtained in Ref. 32, if we ignore effects of dephasing due to oscillator frequency modulation. This is justified since the only source of dephasing in JBA circuits would be due to $1/f$ fluctuations in the critical current of the junction or the dielectric constant of the capacitor, and they are quite small in the frequency range relevant for escape dynamics.

III. DESIGN AND FABRICATION

In this section we will briefly discuss the techniques for fabricating the JBA and some design considerations. In the first step, a metallic underlayer—either a normal metal (Au or Cu) or a superconductor (Nb)—is deposited on a silicon substrate to form one plate of the shunting capacitor. This is followed by deposition of a 200 nm insulating SiN layer by plasma-enhanced chemical vapor deposition at 400 °C. This layer is the dielectric material in the capacitor. Using e-beam lithography and double-angle shadow mask evaporation, we then fabricate the top capacitor plates along with a few square micron sized Al/AlO$_x$/Al tunnel junction. The top capacitor plates along with the metallic underlayer form two capacitors in series. Figure 8 shows an optical image of the on-chip capacitor along with the schematic profile of the ground plane multilayer used for Cu based capacitors. The other metallic layers (Ti and Cr) were employed for protecting the Cu layer during the deposition of the dielectric layer. It also ensured that the Cu layer would adhere properly to the silicon substrate. For Au and Nb underlayers, SiN was directly deposited on top. Also shown in the bottom right corner is a scanning electron microscrope (SEM) image of a typical Josephson tunnel junction. The critical current of the junction was in the range of $I_0 = 1-2\ \mu$A corresponding to a Josephson inductance in the range of $L_J = 0.3-0.15$ nH. By varying both the dielectric layer thickness and the pad area,

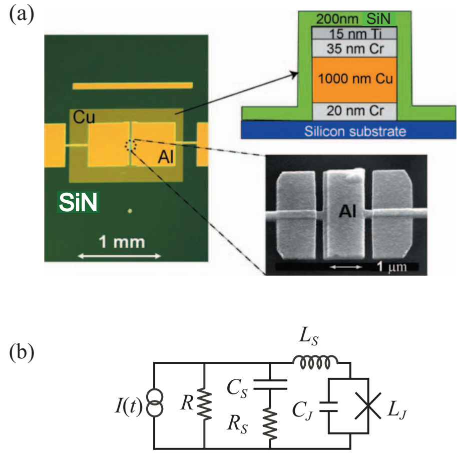

FIG. 8. (Color) Optical image of the microfabricated on-chip capacitor is shown in the left panel. The top Al layer forms two capacitors in series with the Cu underlayer as the common electrode. Top right panel indicates the profile of the different layers in the ground plane. The additional layers (Ti and Cr) sandwiching the Cu layer are used to protect the Cu layer during the deposition of SiN. These additional layers are not required for Nb ground planes. The bottom right panel shows a SEM image of a typical Josephson junction, which is shunted by the capacitor. (b) Circuit schematic of the JBA chip including stray elements. The junction inductance (L_J) is shunted with a capacitor (C_S) including the stray inductance (L_S) and stray resistance R_S. $C_J \ll C_S$ is the intrinsic junction capacitance. The stray inductance and resistance arise due to imperfect screening currents and the finite conductivity of the ground planes.

the total shunt capacitance C_S was varied between 16 and 40 pF. The plasma frequency of the JBA was kept in the range of 1–2 GHz. Several samples were fabricated and their parameters are listed in Table II. For more details on fabrication techniques, including the transmission line version of the JBA, see Ref. 23.

We will now discuss some important design considerations to ensure that a well controlled bifurcation can be observed. In particular, we will discuss the microwave characteristics of the shunting capacitor, which reduces the bare plasma frequency of the Josephson junction. A more generalized discussion on the requirements of the shunting impedance for observing a bifurcation can be found in Ref. 12. The shunting capacitor has to be implemented carefully to ensure that it behaves as a capacitor at the relevant frequencies with minimal parasitic resistance and inductance. At higher frequencies (>5 GHz), it is much easier and practical to use distributed circuit elements such as transmission line resonators. This was one of the driving factors for the development of the CBA, which uses transmission line resonators with an embedded Josephson junction to implement the nonlinear oscillator.[35]

TABLE II. Sample parameters from Ref. 11. $L_J=\varphi_0/I_0$ and ω_{p0} are measured values. C_S and L_S are fit values to the data. Samples 1 and 2 have a 100 nm thick Au underlayer, sample 3 has a 50 nm thick Nb underlayer, samples 4 and 6 have a 1 μm thick Cu underlayer, and sample 5 has a 200 nm thick Nb underlayer.

Sample	L_J (nH)	$\omega_{p0}/2\pi$ (GHz)	C_S (pF)	L_S (nH)	R_S (Ω)
1	0.28	1.18	39 ± 1	0.20 ± 0.02	0.8
2	0.18	1.25	30 ± 4	0.34 ± 0.04	0.8
3	0.32	1.64	16 ± 1	0.27 ± 0.02	$\sim$0.0
4	0.38	1.81	19 ± 1	0.03 ± 0.02	$\sim$0.02
5	0.40	1.54	19 ± 1	0.15 ± 0.02	$\sim$0.0
6	0.28	1.80	27 ± 1	0.01 ± 0.02	$\sim$0.0

The first generation of our microwave capacitors were made using a thin (100 nm) Au ground plane. This was followed by Nb ground planes (50 and 200 nm) and then thick (1 μm) Cu. Imperfect screening currents in the capacitor plates due to the finite conductivity (Au and Cu) and thickness of the ground planes result in a stray inductance (L_S) and a stray resistance (R_S). Figure 8(b) depicts a model that accounts for the stray inductance and resistance. The samples made with superconducting Nb ground planes did not have any stray resistance, while the data for samples with Au and Cu ground planes lead to values of $R_S=0.8$ and 0.02 Ω, respectively. The lowest parasitic inductance $L_S=0.026$ nH was obtained with the 1 μm Cu ground planes, while the other samples had a value in the range of 0.15–0.34 nH. The presence of stray resistance results in dissipation in the oscillator, and the phase shift in the reflected signal upon crossing the resonance is much less than the 360° expected for a lossless oscillator. In the high power regime, the samples with large stray resistance made a transition into a chaotic state before encountering the bistable regime. This chaotic state is also observed in well behaved samples at higher powers (black region in Fig. 13), but there is a large enough range of powers where the bistable regime is observed. The stray inductance has a similar effect as it increases the linearity of the oscillator, thereby pushing the onset of the nonlinear regime to higher drive powers and closer to the chaotic state. To summarize, the stray parameters L_S and R_S reduce and in the worst case eliminate the available phase space where one can observe the bistable regime of the nonlinear oscillator. For the JBA with $Q\sim20$, one should aim to achieve $L_S/L_J<10$ and $R_S/Z_0<10^{-3}$ for optimum results.

IV. EXPERIMENTAL SETUP

The JBA chip is placed on a low-loss microwave circuitboard ($\varepsilon_r=10$) and is wire-bonded to the end of a coplanar stripline, which is soldered to a coaxial launcher affixed to the side wall of the copper sample box. We anchor the rf leak-tight sample box to the cold stage of a dilution refrigerator with base temperature of 15 mK. Some preliminary data were also obtained in a ^{3}He cryostat with a base temperature of 270 mK. The measurement setup including the values of filters and attenuators is shown in Fig. 9.

For frequency domain measurements, microwave excitation signals are generated by a HP 8722D vector network analyzer and are coupled to the sample via the −13 dB side port of a directional coupler after passing through cryogenic attenuators. The reflected microwave signal passes through the direct port of the coupler and is amplified first using a cryogenic 1.20–1.85 GHz high electron mobility transistor (HEMT) amplifier with noise temperature $T_N=4$ K before returning to the network analyzer. The isolators on the return line allow microwave signals to propagate only in one direction and suppress the HEMT amplifier input noise irradiating the sample by 60 dB. To suppress noise outside the band of

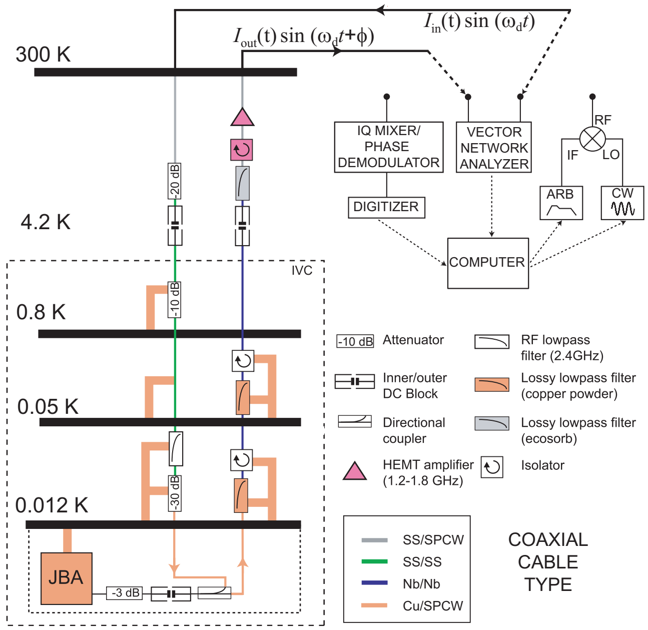

FIG. 9. (Color) Cryogenic microwave measurement setup. The rf excitation line is attenuated and filtered with reactive components. The signal return line has isolators and lossy filters. Typical values of components along with the type of coaxial cables used are indicated.

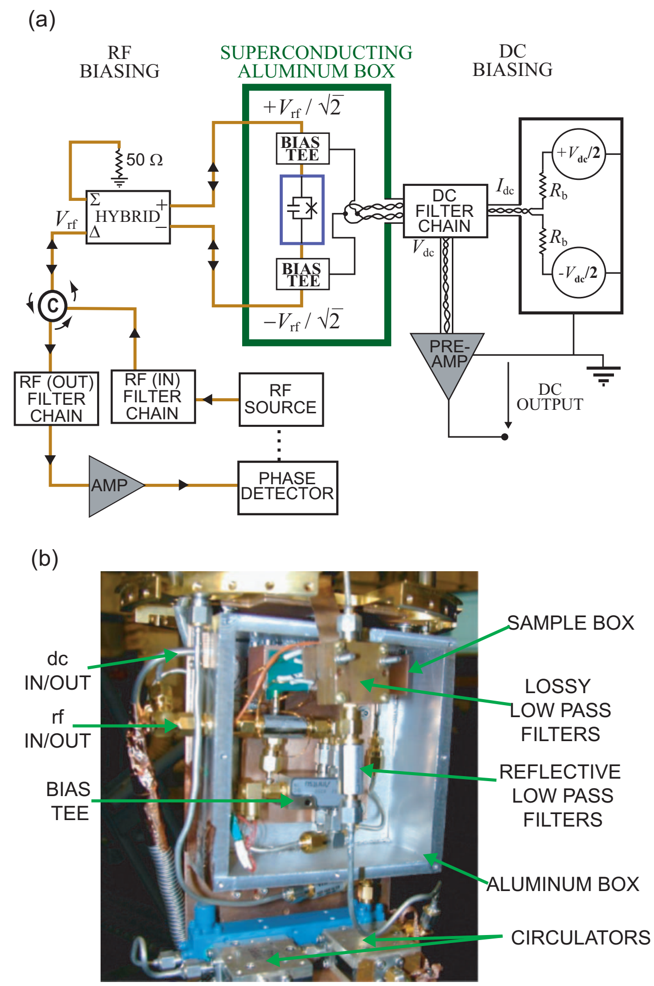

FIG. 10. (Color) Schematic (a) and optical image (b) of the combined differential rf and dc biasing scheme. Shielded twisted-pair wires implement a four wire dc *I-V* measurement. A 180° hybrid coupler is used to split the rf signal into two out of phase components, creating the differential rf drive. The rf and dc signals are combined using a bias tee before they reach the device (inside blue rectangle). A superconducting Al box (green rectangle) is used to shield the device from low frequency magnetic fields since the twisted pairs have to be separated before they can be combined with the rf signals. This differential biasing scheme rejects noise over a wide frequency range.

the isolators (1.20–1.85 GHz), we use lossy transmission line filters.[23,36] The attenuators on the input line carry out a similar function by reducing the noise from higher temperature stages. These components ensure that the intensity of the fluctuations at the sample correspond to the temperature of the cold stage to which it is anchored. This is important for maximizing the sensitivity of the JBA.

For the time domain measurements, we used a Tektronix AWG 520 to create the pulse envelopes. These envelopes were combined with cw microwave signals from a synthesized microwave generator using analog mixers. The reflected signal was then mixed down to a lower frequency and digitized using a 1 GS/s digitizer from Acqiris. The phase was then determined by fitting this demodulated signal in software. Alternatively, we also used an Analog Devices phase detector (AD 8302) for directly converting the reflected signal phase into a voltage. This was the preferred method when the JBA was being used as a digital threshold detector and enabled rapid determination of the oscillation state with no software processing overhead.

For ultralow noise, simultaneous dc and rf measurements on the same JBA sample, we developed a fully differential measurement scheme as shown in Fig. 10. *I-V* characteristic and low frequency switching current measurements[7] are often required to extract system parameters such as the critical current and the effective temperature.[33] Nonequilibrium noise is effectively rejected in low frequency measurements by using twisted-pair cables with fully differential signals. Radio frequency signals on the other hand are traditionally single ended and are susceptible to common mode noise when combining low and high frequency measurements. To remedy this problem, we used a 180° hybrid coupler to create two out of phase rf signals, which were then combined with the dc signals using two bias tees to create a fully differential excitation. This setup was used only for ultralow noise measurements such as the escape temperature measurements in the JBA described at the end of Sec. V B.

V. RESULTS

A. Frequency domain measurements

Frequency domain measurements are used to characterize the nonlinear oscillator and extract circuit parameters. The linear plasma resonance is located by sweeping the excitation frequency ω_d and measuring the reflection coefficient $\Gamma_R(\omega_d)=[Z(\omega_d)-Z_0]/[Z(\omega_d)+Z_0]$. Here $Z_0=50\ \Omega$ is the characteristic impedance of our transmission lines, and $Z(\omega_d)$ is the impedance seen at the sample holder plane. For an ideal *LC* resonator without intrinsic dissipation, we expect a phase shift $\Delta\phi=\phi_{\omega_d\gg\omega_{p0}}-\phi_{\omega_d\ll\omega_{p0}}=2\pi$. The excitation power was kept low enough to access the linear regime of the oscillator. In Fig. 11, we present the reflected signal

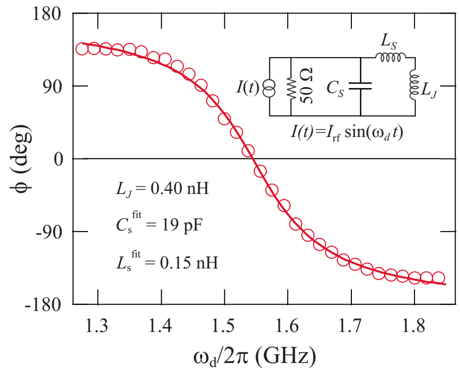

FIG. 11. (Color online) Normalized reflected signal phase ϕ as a function of excitation frequency $\omega_d/2\pi$ for sample 5. The open circles are measured data for $L_J=0.40$ nH. The solid line is calculated from the equivalent circuit model shown in the inset. The magnitude of the reflected signal is unity within experimental uncertainty.

phase ϕ as a function of excitation frequency for sample 5. The point where $\phi=0$ is the linear-regime plasma frequency. For sample 5, $\omega_{p0}/2\pi=1.54$ GHz.

The precise frequency and critical current dependence of the reflected signal phase of our samples can be explained by the lumped element model shown in Fig. 8(b). The plasma frequency in the linear regime is determined by the total inductance L_J+L_S and capacitance C_S and is given by the following relation:

$$\left(\frac{1}{\omega_{p0}}\right)^2 = C_S(L_J+L_S) = \frac{\varphi_0 C_S}{I_0} + C_S L_S. \tag{17}$$

A plot of $(2\pi/\omega_{p0})^2$ versus $1/I_0=L_J/\varphi_0$ is shown in Fig. 12 for samples 1, 2, 4, and 5. As the critical current is decreased by applying a magnetic field in the plane of the junction, its inductance increases, and the plasma frequency is reduced. For each sample, a linear fit to the data of Fig. 12 yields the values of C_S and L_S (see Table II). The fit values for C_S agree well with simple estimates made from the sample geometry.

For samples with a thin underlayer (1–3), a stray inductance in the range $L_S=0.20-0.34$ nH was observed. For samples 4 and 5 with a significantly thicker underlayer, L_S was reduced to 0.026 and 0.15 nH, respectively. This behavior is consistent with the calculated screening properties of

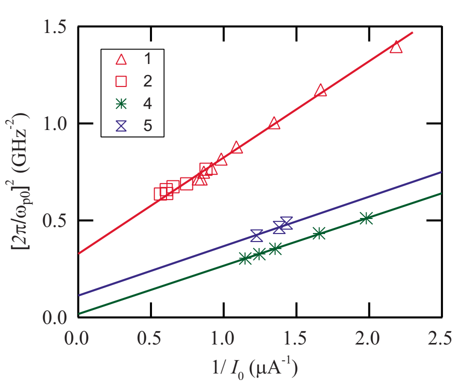

FIG. 12. (Color online) Inverse squared of the plasma frequency $(2\pi/\omega_{p0})^2$ as a function of the inverse critical current $1/I_0$ for samples 1, 2, 4, and 5. Solid lines are linear fits to the data corresponding to the model in Fig. 11 with a single best fit line drawn for samples 1 and 2, which nominally differ only in I_0.

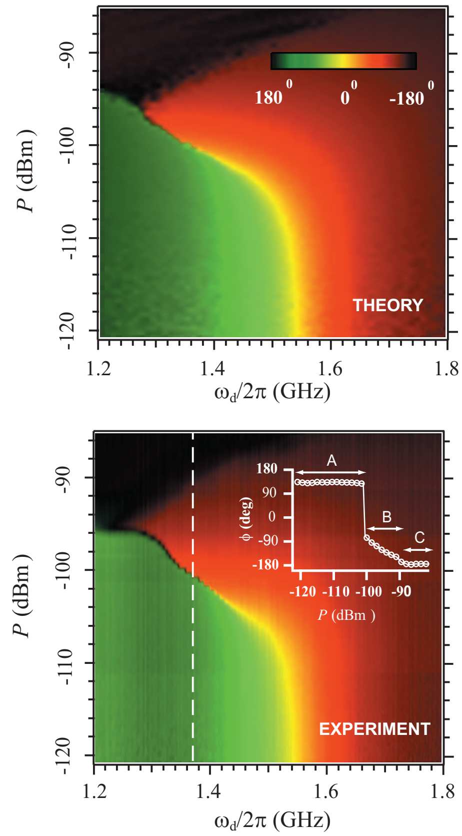

FIG. 13. (Color) Normalized reflected signal phase ϕ as a function of excitation frequency $\omega_d/2\pi$ and excitation power P is shown for sample 5. Experimental data are shown in the bottom panel, while the top panel is the result of numerical simulations. A vertical slice taken at $\omega_d/2\pi$ =1.375 GHz (dashed line) shows the abrupt transition between two oscillation states of the system.

our thin films. Using L_S and C_S we can accurately predict the observed resonant line shape (solid line) in Fig. 11 in which $R_S\sim 0$. Samples with a normal underlayer yielded finite values of R_S.

We now discuss measurements of the power dependence of the plasma resonance. The reflected signal phase as a function of frequency for increasing power for sample 5 is presented in the lower panel of Fig. 13 as a two dimensional color plot. Each row is a single frequency sweep, similar to Fig. 11. For small excitation power, we recover the linear plasma resonance at 1.54 GHz, indicated in yellow, corresponding to $\phi=0$. As the incident power is increased beyond −115 dBm, the plasma frequency decreases as explained in Sec. II. For powers greater than −105 dBm, there is an abrupt transition from the phase leading (green) to phase lagging (red) state. This marks the transition from the low amplitude state to the high amplitude state. One can cross this transition by sweeping the power at fixed frequency also (dashed line). For powers in excess of −90 dBm, we encounter a new dynamical regime (black region in Fig. 13) where δ appears to diffuse between the wells of the cosine potential. This was confirmed by the presence of an unambiguous audio frequency ac resistance in the black region (see Ref. 20). In the lower panel of Fig. 13 (inset), we illustrate the sequence of dynamical transitions by plotting ϕ as a function of incident power at $\omega_d/2\pi=1.375$ GHz. For $P<$

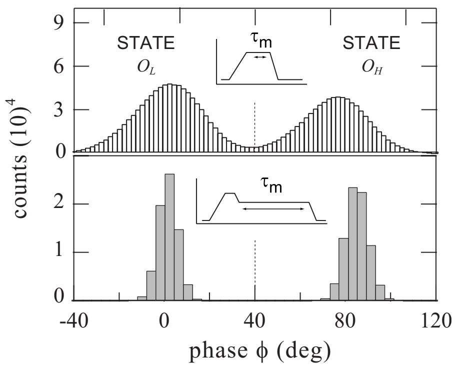

FIG. 14. Histograms of the reflected signal phase at $I_{rf}/I_0=0.145$. The upper histogram contains 1.6×10^6 counts with a measurement time $\tau_m=20$ ns. The lower panel, taken with the latching technique, has 1.5×10^5 counts with a measurement time $\tau_m=300$ ns. The dashed line represents the discrimination threshold between the O_L and O_H states.

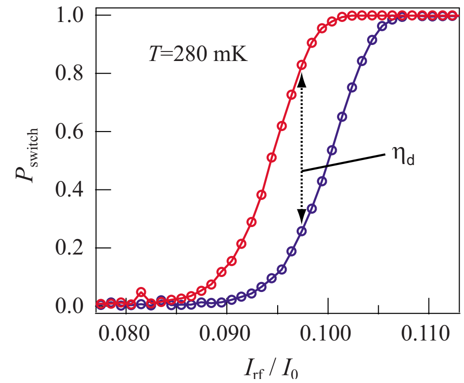

FIG. 15. (Color online) Switching probability curves at $T=280$ mK as a function of the normalized drive current I_{rf}/I_0. The discrimination power η_d is the maximum difference between the two curves. The two curves differ by approximately 1% in I_0, and the curve corresponding to the higher critical current lies at higher values of I_{rf}/I_0.

-102 dBm, the phase is independent of power and δ oscillates in a single well in the harmonic-like phase leading state (letter A). For $-102\ \text{dBm} < P < -90$ dBm, the phase evolves with power and δ still remains within the same well but oscillates in the anharmonic phase lagging state (letter B). Finally, for $P > -90$ dBm, the average phase of the reflected signal saturates to $-180°$, corresponding to a capacitive short circuit. This last value is expected if δ hops randomly between wells, the effect of which is to neutralize the Josephson inductance.

To explain the complete frequency and power dependence of the transitions shown in the lower panel of Fig. 13, we numerically solved the full circuit model shown in Fig. 8(b), including the exact sinusoidal junction current-phase relation. The result of this calculation is shown in the upper panel of Fig. 13. It correctly predicts the variation in the plasma frequency with excitation power and the boundaries of the phase diffusion region. The agreement between theory and experiment is remarkable in view of the simplicity of this model, which uses only measured parameters.

B. Time domain measurements

The measurements described so far characterized the time averaged response of the Josephson oscillator under continuous microwave excitation. We will now describe the experiments that probed the dynamics of the JBA at short time scales ($\sim$10 ns) under pulsed microwave excitation. Data from sample 6 are presented in this section.

We first characterized in detail the switching associated with the $O_L \to O_H$ transition near the bifurcation point I_B^+. We excited the oscillator with two different readout pulse protocols. In the first protocol, the drive current was ramped from zero to its maximum value in 40 ns and was then held constant for 40 ns before returning to zero. Only the final 20 ns of the constant drive period were used to determine the oscillation phase ϕ with the first 20 ns allotted for settling of the phase. Histograms taken with a 10 MHz acquisition rate are shown in Fig. 14. In the upper panel, the two peaks corresponding to states O_L and O_H can be easily resolved with a small overlap of 10^{-2}. The finite width of each peak is due to the output noise and is consistent with the system noise temperature of our microwave electronics. In this first method, the latching property of the system has not been exploited. In the second protocol for the readout pulse, we again ramp for 40 ns and allow a settling time of 20 ns, but we then reduce the drive current by 20% and measure the reflected signal for 300 ns. In that latter period, whatever state was reached at the end of the initial 60 ns period is "latched" and this time is used to improve the signal/noise ratio of the reflected phase measurement. As shown in the lower panel of Fig. 14, the two peaks are now fully separated, with an overlap of 6×10^{-5}, allowing a determination of the state O_H probability with an accuracy better than 10^{-3}. This second protocol is well suited to precise time-resolved measurements of I_0 or for applications where a low noise follower amplifier is unavailable. At the end of the pulse, the amplitude is ramped back to zero in 10–20 ns. The ramp up and ramp down times depend on the quality factor of the resonator, and we ensure that this process is adiabatic and there is no ringing in the oscillator. This entire process can be repeated almost immediately since there is no heating due to the absence of on-chip dissipation leading to very fast repetition rates ($\lesssim 10$ MHz).

We then measured the switching probability curves or S-curves, $P_{switch}(I_{rf})$, for different values of I_0 to evaluate the sensitivity of the JBA. Using the readout protocol and the discrimination threshold shown in Fig. 14, we obtain the switching probability curves shown in Fig. 15. Defining the discrimination power η_d as the maximum difference between two S-curves, which differ in I_0, we find that at $T=280$ mK, $\eta_d=57\%$ for $\Delta I_0/I_0=1\%$. The switching probability curves should shift according to $(\Delta I_B/I_B)/(\Delta I_0/I_0)=3/4\alpha$ [Eq. (7)], which for our case takes the value of 6.1. In Fig. 15, the curves are shifted by 6%, which agrees well with this prediction.

As discussed in Sec. II, the width of the S-curves depends on the effective intensity of fluctuations in the JBA oscillator. A well designed experimental setup will ensure that this intensity of fluctuations is set by the thermal/quantum fluctuations corresponding to the operating temperature of the JBA. It is possible to determine the effective temperature characterizing these fluctuations by measuring the escape rate from state O_L to O_H as a function of the various bias parameters. The classical theory of escape was briefly described in Sec. II. In the quantum regime $T \ll \hbar\omega_{p0}/k_B$, the effective intensity of fluctuations is given by setting $T=T_{\rm eff}=\hbar\omega_{p0}/2k_B$.[30,31] The full expression for the escape temperature[34] is given by Eq. (16).

We will now describe the procedure for measuring the escape rate from the low amplitude state of the JBA. The JBA was biased with a long trapezoidal pulse at frequency ω_d with amplitude $I_{\rm rf}$. The pulse ramp time used was 40 ns. The total pulse length was 1 ms. The phase of the reflected pulse is analyzed and the time ($\tau_i^{\rm switch}$) at which the JBA makes a transition from low to high amplitude state is recorded. The experiment is repeated typically for $N=10^5$ times. We then construct the probability $P_L(\tau)$ of the JBA being the low amplitude state as

$$P_L(\tau) = 1 - \frac{1}{N}\Sigma_{i=1}^{N}\Theta(\tau - \tau_i^{\rm switch}), \tag{18}$$

where

$$\Theta(\tau) = 0 \quad \tau < 0$$

$$= 1 \quad \tau \geq 0 \tag{19}$$

is the Heaviside unit step function. The probability $P_L(\tau)$ decays exponentially with a decay constant given by the escape rate $\Gamma_{\rm esc}^{\rm rf}$,

$$P_L(\tau) = \exp(-\Gamma_{\rm esc}^{\rm rf}\tau). \tag{20}$$

So by fitting an exponential to $P_L(\tau)$, we can determine $\Gamma_{\rm esc}^{\rm rf}(I_{\rm rf})$ for different bias amplitudes $I_{\rm rf}$. The results are shown in Fig. 16 where we have plotted the reduced escape rate $\tilde{\Gamma}_{\rm esc}^{\rm rf}(I_{\rm rf})=[\log(\omega_a/2\pi\Gamma_{\rm esc}^{\rm rf})]^{2/3}$ given by

$$\tilde{\Gamma}_{\rm esc}^{\rm rf}(I_{\rm rf}) = \left(\frac{U_{\rm esc}^{\rm rf}}{k_B T_{\rm esc}^{\rm rf}}\right)^{2/3}\left(1 - \frac{I_{\rm rf}^2}{I_B^2}\right) \tag{21}$$

as a function of $I_{\rm ef}^2/I_B^2$ for selected values of bath temperatures. Data are shown for two samples with different resonant frequencies in panels (a) and (b).

We observe straight lines with different slopes for different bath temperatures. The slope $\tilde{\Gamma}_{\rm slope}$ and intercept $\tilde{\Gamma}_{\rm int}$ of the line are given by

$$\tilde{\Gamma}_{\rm slope} = -\left(\frac{U_{\rm esc}^{\rm rf}}{k_B T_{\rm esc}^{\rm rf}}\right)^{2/3}\frac{1}{I_B^2}, \tag{22a}$$

$$\tilde{\Gamma}_{\rm int} = \left(\frac{U_{\rm esc}^{\rm rf}}{k_B T_{\rm esc}^{\rm rf}}\right)^{2/3}. \tag{22b}$$

From these two quantities we can determine the bifurcation current I_B and escape temperature $T_{\rm esc}^{\rm rf}$ using the following formulae:

$$I_B = (-\tilde{\Gamma}_{\rm int}/\tilde{\Gamma}_{\rm slope})^{1/2}, \tag{23a}$$

$$T_{\rm esc}^{\rm rf} = \frac{U_{\rm esc}^{\rm rf}}{k_B \tilde{\Gamma}_{\rm int}^{3/2}}. \tag{23b}$$

This confirms that the escape rate follows the behavior given by Eqs. (8) and (9). We can then extract the escape temperature $T_{\rm esc}^{\rm rf}$ for each operating point. Note that in the experiment, we control $I_{\rm rf}$ by varying the pulse amplitude ($A_{\rm rf}$) of the rf generator. Since $I_{\rm rf}\propto A_{\rm rf}$, we can plot $\tilde{\Gamma}_{\rm esc}^{\rm rf}$ as a function of $A_{\rm rf}^2$ and extract the bifurcation amplitude ($A_B \propto I_B$) using Eq. (23a). Once we have A_B we can plot the data as a function of $A_{\rm rf}^2/A_B^2$, which is the same as $I_{\rm rf}^2/I_B^2$. When plotted this way, the straight lines should intersect $\tilde{\Gamma}_{\rm esc}^{\rm rf}=0$ at $I_{\rm rf}^2/I_B^2=1$ at all temperatures since the bifurcation current I_B (and hence A_B) does not depend on temperature. The data for each temperature in Fig. 16 have been plotted after normalizing the x-axis with the value of I_B (A_B) extracted at the lowest temperature. In practice, we always observe small differences in the extracted values of A_B at different temperatures as is evident from the data. This could imply that the data start to deviate from the prediction of Eq. (8). However we found that this variation was predominantly due to the slow increase in the attenuation of the input coaxial lines due to slowly decreasing levels of liquid Helium in the dewar of the dilution refrigerator. We observed that the extracted values of A_B always increased with time even when the temperature was kept constant and reverts back when the liquid helium level is restored. The data shown in Fig. 16 take about 2 days to acquire since one has to wait for the system to thermalize at each operating temperature. During such long periods, the

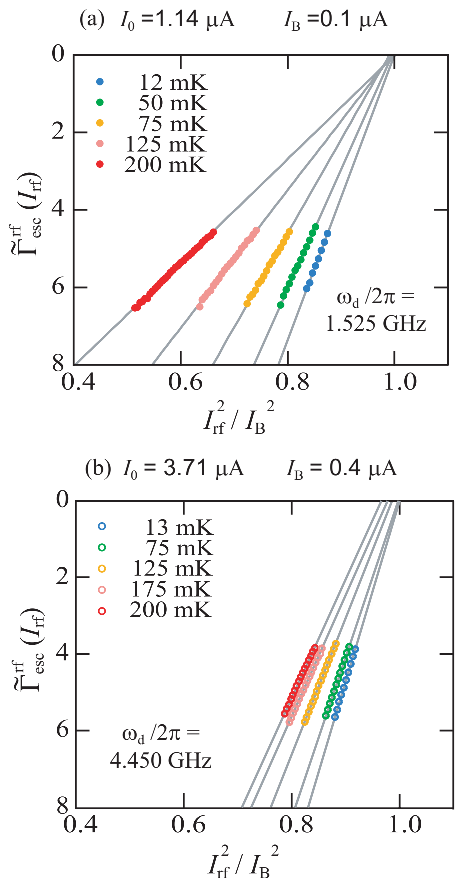

FIG. 16. (Color) The reduced escape rate $\tilde{\Gamma}_{\rm esc}^{\rm rf}(I_{\rm rf})$ as a function of $I_{\rm rf}^2/I_B^2$ at different bath temperatures (decreasing from left to right). Data are shown for two samples with (a) $\omega_p/2\pi=1.670$ GHz and $\omega_d/2\pi=1.525$ GHz and (b) $\omega_p/2\pi=4.690$ GHz and $\omega_d/2\pi=4.450$ GHz. The solid lines are straight line fits to the data. The slope and intercept of these fits are used to extract the escape temperature $T_{\rm esc}^{\rm rf}$ and the bifurcation current I_B^+.

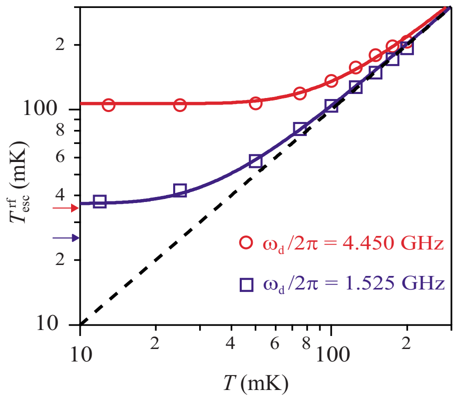

FIG. 17. (Color online) T_{esc}^{rf} vs T obtained from the data in Fig. 16. The solid lines are a plot of Eq. (16) for $\omega_d/2\pi$=1.525 GHz and $\omega_d/2\pi$ =4.450 GHz, respectively. Data show excellent agreement with the theoretical prediction. The dashed line is the classical dependence $T_{esc}^{rf}=T$. The arrow indicates the lowest escape temperature measured in the dc escape measurements for the corresponding sample.

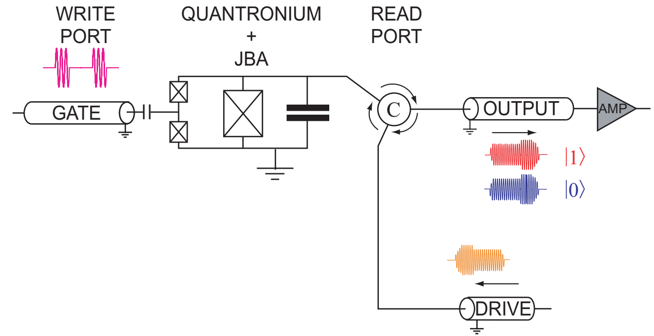

FIG. 18. (Color) Schematic of the qubit measurement setup. The quantronium qubit is comprised of two small Josephson junctions and a large junction in a loop. This latter junction is shunted by a capacitor and forms the nonlinear oscillator of the JBA. The qubit state is manipulated by sending pulses to the gate (write port), while readout operation is performed by sending a pulse to the nonlinear resonator via the read port. The circulator (C) is used to separate the incident and reflected signals. The phase of the reflected signal carries information about the qubit state.

liquid helium level can change appreciably. We also verified that the extracted values of A_B remained constant when noise was added to the system to artificially elevate the temperature. All these checks were done to ensure that our experiment follows the prediction of Eq. (8) and we can extract meaningful results for the value of T_{esc}^{rf}.

In order to extract T_{esc}^{rf} from the data, we need the value of U_{esc}^{rf}. Data from numerical simulations of the JBA circuit yielded a value for U_{esc}^{rf} which was 10%–20% larger than those obtained from Eq. (9b). This would lead to a 10%–20% smaller value for T_{esc}^{rf}, and we observed this discrepancy in the experiments. In order to overcome this problem, we used the following procedure to extract U_{esc}^{rf} from the data itself. At the highest temperature point, we assumed $T_{esc}^{rf}=T$ since that is the expected result in the classical regime.[24] We can then use Eq. (23b) to extract $U_{esc}^{rf}=k_B T_{esc}^{rf}\tilde{\Gamma}_{int}^{3/2}$. This extracted value of U_{esc}^{rf} is then used for all the lower temperature points. This is valid provided we can ensure that the intensity of fluctuations in the JBA really correspond to the thermal fluctuations at that temperature. We verified this by biasing the junction with a dc current and measuring the escape rate from the superconducting to the normal state of the junction. We used the procedure described in Ref. 33 to measure the escape rates $\Gamma_{esc}^{dc}(I_{dc})$ and extract the dc escape temperature T_{esc}^{dc} and found that the escape temperature varied linearly with bath temperature at high temperatures. For our sample parameters, the relation $T_{esc}^{dc}=T$ should be satisfied down to the lowest temperature of our fridge (12 mK). We only observed a small discrepancy at the lowest temperatures, which we attribute to improperly thermalized filters and unfiltered noise in the dual (dc+rf, Fig. 10) biasing configuration. The blue and red arrows in Fig. 17 indicate the smallest value of T_{esc}^{dc}. Nevertheless, the dc escape temperature data validate our normalization procedure described above.

Figure 17 plots T_{esc}^{rf} extracted from the data shown in Fig. 16 as a function of bath temperature T. The solid lines are a plot of Eq. (16) with the corresponding values of ω_d used in the measurement. The agreement between theory and experiment is excellent for both the samples with different resonant frequencies. Note that this is not a fit to the data. The only scaling of data performed, as explained above, is the extraction of U_{esc}^{rf} from the highest temperature data point for each sample. The results for T_{esc}^{rf} not only agree with theory for the lowest temperature point, but the functional dependence on temperature as we cross over from the classical ($k_BT\gg\hbar\omega_d$) to quantum regime ($k_BT\ll\hbar\omega_d$) is also well reproduced. This verifies that the sensitivity of the JBA when operated as a digital threshold detector is only limited by quantum fluctuations.

VI. APPLICATIONS

A. Qubit readout

Superconducting quantum bits (qubits) are electronic circuits with discrete energy levels and are thus "artificial atoms."[37–41] As discussed in Sec. II, the transition from the low amplitude state to the high amplitude state of the JBA depends sensitively on the critical current of the junction. This can be used to readout the state of superconducting qubits. We engineer the circuit such that the two quantum states of the qubit differ sufficiently in critical current to induce switching in the JBA when it is biased in the bistable regime. This approach has been applied to charge-phase,[42] flux,[43] and transmon qubits[44] and is currently being explored in phase[45] qubits as well. We detail measurements of a quantronium qubit[39] using the readout protocol depicted in Fig. 18. The qubit and the JBA are phase coupled via the large junction. The desired qubit state is prepared by applying the appropriate microwave pulses to the write port. The readout operation is performed by applying microwave pulses to the read port, which energizes the JBA oscillator. Biasing the JBA near its bifurcation point encodes the qubit state in the oscillation state of the JBA. The latter is ascertained by analyzing the reflected signal phase. Repeated measurements are then used to obtain the probability of switching from the low amplitude to the high amplitude state. The measurement is arranged so that the switching probability is close to zero when the qubit is in its ground state, while the switching probability is close to one when the qubit is in its first excited state. Ideally, we would like the switching probability to be zero for qubit ground state and one for qubit excited state.

Neglecting the dissipation induced in the transmission lines, the total Hamiltonian of the quantronium coupled to a JBA resonator is $\hat{H}(t)=\hat{H}_{\text{box}}(t)+\hat{H}_{\text{res}}(t)$ (Ref. 42) with

$$\hat{H}_{\text{box}}(t)=4E_C\left[\hat{N}-\frac{1}{2}+\frac{C_gU(t)}{2e}\right]^2-\left(E_J\cos\frac{\hat{\delta}}{2}\right)\cos\hat{\theta}, \tag{24}$$

$$\hat{H}_{\text{res}}(t)=\frac{\hat{q}^2}{2C_s}-E_J^R\cos\hat{\delta}-\varphi_0 I(t)\hat{\delta}.$$

This Hamiltonian has been written supposing that the asymmetry between the two small junctions is zero and the dc values of the offset gate charge and loop flux have been adjusted to operate at the degeneracy point, i.e., $C_gU/2e=1/2$ and zero flux in the loop.[39] Here, $\hat{N}$ and $\hat{q}/2e$ are the momenta conjugate to the generalized positions $\hat{\theta}$ and $\hat{\delta}$, respectively. The control parameters $U(t)=U_{\text{rf}}(t)\cos\omega_{\text{rf}}t$ and $I(t)=I_{\text{rf}}(t)\sin\omega_d t$ are analogous to electromagnetic probe fields in an atomic system and induce a charge excitation of the write port and a phase excitation of the read port, respectively. If we keep these two lowest states in the Hilbert space of $\hat{H}_{\text{box}}$ (Ref. 46) and we express $\hat{H}_{\text{res}}$ in terms of the photon creation and annihilation operators, we obtain an effective Hamiltonian

$$\hat{H}_{\text{eff}}=\frac{2C_gU(t)}{e}E_C\sigma_X-\frac{E_J}{2}\sigma_Z+\hbar\omega_{p0}(1+\lambda\sigma_Z)a^\dagger a$$
$$-\mu\left(1+\frac{\lambda}{4}\sigma_Z\right)(a+a^\dagger)^4-f(a+a^\dagger)I(t), \tag{25}$$

where

$$\omega_{p0}=\sqrt{\frac{E_J^R}{\varphi_0^2C_S}}, \tag{26a}$$

$$\lambda=\frac{E_J}{4E_J^R}, \tag{26b}$$

$$\mu=\frac{E_C^R}{12}=\frac{1}{12}\frac{(e)^2}{2C_S}, \tag{26c}$$

$$f=\varphi_0\left(\frac{2E_C^R}{E_J^R}\right)^{1/4}. \tag{26d}$$

The photon annihilation operator a is related to $\hat{\delta}$ by

$$\hat{\delta}=\frac{a+a^\dagger}{(E_J^R/2E_C^R)^{1/4}}, \tag{27}$$

which represents the decomposition of the gauge-invariant phase difference into annihilation and creation operators of the "plasma" mode whose bare frequency is ω_{p0}. The operators σ_X and σ_Z are the Pauli spin operators, and $E_C^R=e^2/(2C_S)$ is the single electron charging energy of the readout junction. In this effective Hamiltonian, the expansion of $\cos\hat{\delta}$ is carried out only to the first anharmonic term, which describes the nonlinear resonator dynamics with sufficient accuracy for a bifurcation readout.

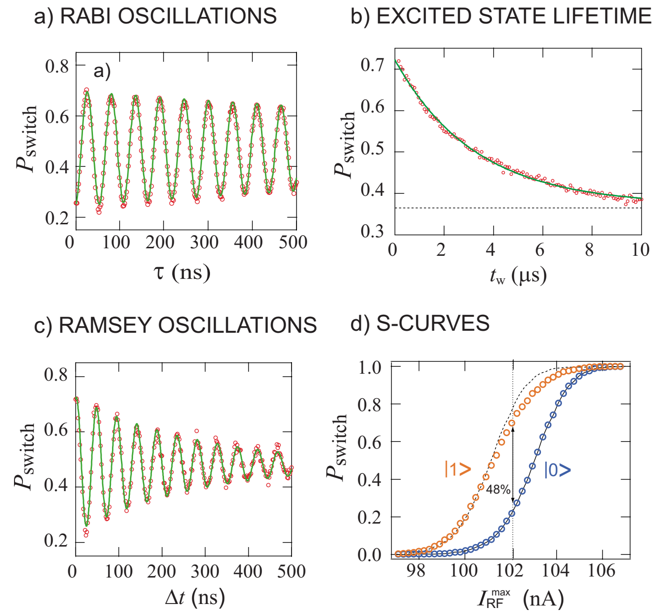

FIG. 19. (Color online) Summary of qubit coherence measurements. The Larmor frequency of the qubit is 9.513 GHz with $E_J/E_C=2.7$. (a) Rabi oscillations as a function of the duration τ of a square pulse applied on the gate. Solid green curve is an exponentially decaying sinusoidal fit with $\tilde{T}_2=1.6$ μs. (b) Decay of the excited state, prepared by applying a π pulse, as a function of the waiting time t_w between the preparation and readout pulses. Solid green curve is an exponential fit with a decay constant $T_1=3.2$ μs. The dashed black line indicates the value of P_{switch} in the absence of a π pulse. (c) Ramsey fringes obtained with two $\pi/2$ pulses separated by the time interval Δt. The pulse frequency was detuned from the Larmor frequency by 20 MHz. The green curve is an exponentially decaying sinusoidal fit. The decay time T_2^* is 320 ns. (d) Switching probability as a function of drive current amplitude for ground and excited qubit states. The vertical dotted line is the value of the drive current at which the maximal difference in P_{switch} is observed. The solid line connects the observed data points in the $|0\rangle$ state, and the dashed line is a copy of the solid line horizontally shifted to overlap the $|1\rangle$ state data at low values of P_{switch}.

We now describe the role of each term in Eq. (25). The first term describes the influence on the qubit of the charge port drive, which is used to manipulate its state. The second term describes the free evolution of the qubit at the Larmor frequency $\omega_{01}=E_J/\hbar$. We have supposed here that the ratio E_J/E_C is sufficiently small that corrections to the Larmor frequency involving E_C are small. To model the behavior of qubit samples with an appreciable E_J/E_C ratio, we would keep higher order terms, yielding renormalized values of the coefficients in Eq. (25). The third term describes the dominant coupling between the qubit and the resonator and results in the qubit state affecting the resonant frequency of the resonator. Note that this term commutes with the Hamiltonian of the qubit when $U=0$, offering the possibility of quantum nondemolition measurements.[47] The fourth term is the consequence of the nonlinearity of the resonator and leads to a decrease in the frequency of the resonator when its photon population increases as discussed earlier in Sec. II. Finally, the fifth term describes the excitation of the resonator by the drive current applied through the read port.

The coherence properties of different qubit samples were measured and typical results are shown in Fig. 19. Panel (a) shows the Rabi oscillation data. The Rabi decay time $\widetilde{T}_2$ was found to be in the range 0.8–1.7 μs depending on the sample and precise biasing conditions. A linear dependence of the Rabi oscillation frequency ν_{Rabi} with the microwave drive amplitude $U_{\mathrm{rf}}^{\max}$ was observed, in agreement with the theory of driven two level quantum systems. Panel (b) shows the decay of the excited state lifetime (T_1) with typical lifetimes being in the range of 1–5 μs. The values of T_1 obtained with our dispersive readout are comparable with the results of Vion *et al.*[39] but are significantly shorter than the values expected from coupling to a well thermalized 50 Ω microwave environment shunting the qubit. The loss mechanisms giving rise to the observed energy relaxation are not understood at this time. Panel (c) shows the Ramsey oscillation data, which allow one to measure the decay time of qubit phase coherence during free evolution of the qubit state. Typical Ramsey decay times observed were $T_2 \sim 300$ ns. The Ramsey fringes decay time T_2 has a component due to energy relaxation and one due to pure dephasing: $1/T_2 = 1/(2T_1) + 1/T_\varphi$, where T_φ represents pure dephasing. In our measurements, T_2 is usually dominated by pure dephasing, which is due to fluctuations in the qubit transition frequency originating from $1/f$ offset charge noise. Recent qubit measurements using the cavity version of the JBA show that the dephasing times are compatible with the magnitude of the typical $1/f$ offset charge noise seen in these systems.[13] Immunity to $1/f$ charge noise can be achieved by increasing the E_J/E_C ratio in these qubits, and we observed some improvement in the pure dephasing time for such samples. This strategy is implemented in new qubit implementations, which use very large E_J/E_C ratios to almost eliminate the gate charge dependence of the transition frequency.[41,48]

Panel (d) shows the *S*-curves corresponding to the qubit being in the ground and excited states. The open circles in blue and red correspond to data for the qubit ground and excited states, respectively, while the solid black line is the best fit through the ground state data. The dashed black line is a shifted version of the solid black line to match the excited state data for low switching probabilities. This was done to indicate the small difference in the shape of the excited state *S*-curve resulting in the reduction in readout contrast. The observed contrast for this data is about 15%–30% smaller than expected. In a set of experiments described in Ref. 20, we used two readout pulses in succession to determine that a 15%–30% loss of qubit population occurs even before the resonator is energized to its operating point. We attribute this loss to spurious on-chip defects.[49] As photons are injected into the resonator, the effective qubit frequency is lowered due to a Stark shift via the phase port.[50] When the Stark shifted frequency coincides with the frequency of an on-chip defect, a relaxation of the qubit can occur. Typically, the qubit frequency samples 200–300 MHz before the state of the qubit is registered by the readout, and three to four spurious resonances are encountered in this range. Presently, this phenomenon seems to be limiting the qubit measurement fidelity. The detailed back-action of the JBA on the qubit is still not fully understood and is a topic of current research.[51]

B. High speed magnetometry

As discussed in Sec. I, one can replace the single junction in the JBA with a two junction SQUID to make a sensitive flux detector. Magnetic flux coupled to the SQUID loop modifies its effective critical current and hence can be detected using the JBA principle. There are several modes in which such a magnetometer can be operated. Biasing in the hysteretic regime permits a digital readout, similar to the qubit measurements described above, and could potentially be used for spin state measurements of magnetic molecules. It is also possible to bias in the vicinity of the bifurcation point where the response is nonhysteretic, but the nonlinearity boosts sensitivity. Such a device can detect fast flux changes, which can be used to study the dynamics of nanomagnets.[52]

It is important to distinguish a JBA magnetometer from a conventional dc SQUID device and other rf biased SQUIDs. In the dc SQUID, the magnetometer is biased near the resistive transition where the static voltage is used to register flux coupled to the SQUID loop. A shunt resistor is used to suppress hysteresis in the current-voltage characteristic. Such devices can exhibit bandwidth in excess of 100 MHz with $\mu\Phi_0$ sensitivity[53] but at the expense of dissipation in and around the SQUID. The JBA magnetometer is an inductive device in which the magnitude of the phase excursion δ is always less than π, thus avoiding the dissipation and back-action associated with switching into the voltage state. As such, flux sensitivity alone is not sufficient to compare these two types of magnetometers as their measurement back-action is very different. Radio frequency biased SQUIDs (Ref. 54) do not generate a static voltage but typically do have phase excursions beyond a single well of the washboard potential and the associated back-action. SQUIDs have also been operated in the inductive mode,[55,56] typically where the phase excursion is very small and the anharmonicity of the SQUID potential is not sampled. In the JBA magnetometer, we discuss a device where the quality factor is kept low for enhanced bandwidth and the SQUID is biased near the bifurcation point for enhanced sensitivity.

We built a rf magnetometer by embedding a tunnel junction SQUID in a $\lambda/4$ coplanar stripline resonator. The principle of operation is exactly the same as the lumped element version with a slight difference in the effective circuit.[13]

Figure 20(a) shows a schematic of this circuit, and images of the magnetometer are shown in Fig. 20(b). The device was fabricated using standard e-beam lithography with device parameters chosen to yield a resonant frequency of 1.35 GHz when the flux through the SQUID loop is zero. The quality factor Q of the resonator was around 800. A superconducting coil was used to apply a dc magnetic flux to bias the SQUID. An on-chip coplanar waveguide transmission line with a short circuit termination was used to couple high frequency signals to calibrate the device. The sample box along with the bias coil was enclosed in a superconducting aluminum box to shield from magnetic noise. The microwave measurement setup was similar to the one shown in Fig. 9 but had additional lines to bias the coil and the on-chip flux line.

The reflected signal phase as a function of the bias flux

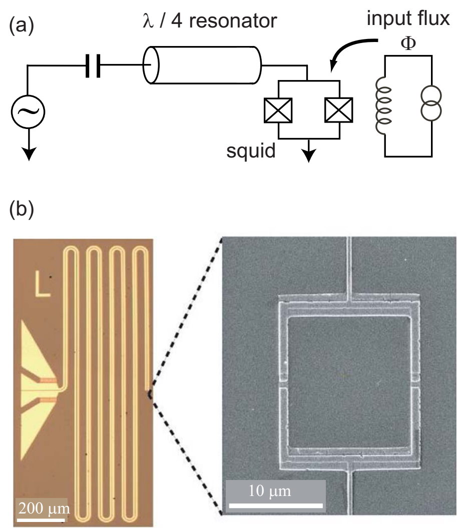

FIG. 20. (Color online) (a) Schematic of a λ/4 resonator terminated with an unshunted two junction SQUID. The input flux applied via a coil modulates the critical current of the SQUID, resulting in a shift in the resonant frequency. (b) Optical image of Al coplanar stripline resonator terminated with an unshunted SQUID, shown in the SEM image on the right.

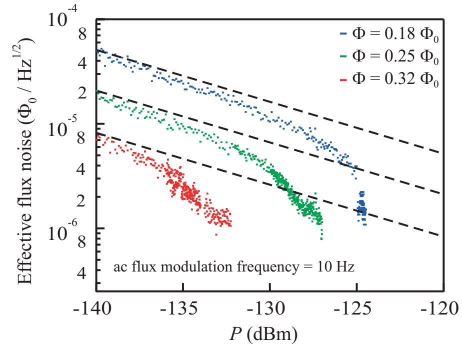

FIG. 22. (Color) Effective flux noise of the magnetometer as a function of drive power. This quantity is the smallest change in the flux one can detect in a 1 Hz bandwidth. Data are shown for a different sample than the one in Fig. 21. The dotted curves (from top to bottom) correspond to data for three increasing values of dc flux bias points. Lowest effective flux noise obtained is 1 $\mu\Phi_0/\sqrt{\text{Hz}}$. The dashed lines indicate the expected reduction in flux noise with power for a comparable linear resonator. Biasing in the nonlinear regime yields an order of magnitude reduction in flux noise.

and drive frequency is shown in the inset of Fig. 21. As expected, we observe the periodic dependence of the resonance frequency (yellow color corresponding to zero phase) as a function of bias flux. The reflected signal phase is plotted as a function of drive power and frequency in Fig. 21 and characterizes the nonlinear response of the resonator. This plot is similar to Fig. 13, but here the power was swept in both directions for a given frequency. The different sweep directions are interlaced in the plot. The sweep direction only affects the hysteretic regime as observed in the striped region in the top left part. One can clearly see the upper and lower bifurcation points. For magnetometry, the device was operated in the linear and the single-valued nonlinear regime by adjusting the microwave power. Small changes in input flux are converted into small changes in the phase of the microwave signal reflected from the resonator, forming the basis of detection. In this technique, the noise temperature of the microwave electronics sets the phase resolution and ultimately determines the magnetometer sensitivity. In the linear regime, the dominant noise contribution comes from the cold HEMT amplifier assembly which has a system noise temperature of about 10 K.

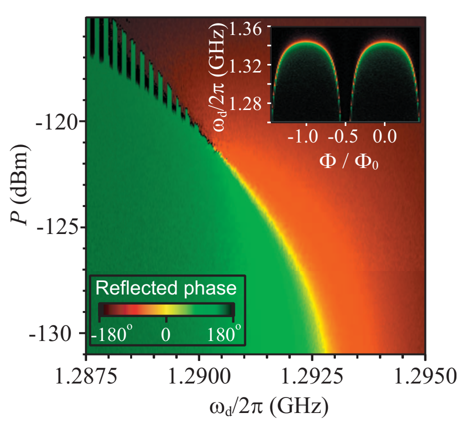

FIG. 21. (Color) Reflected signal phase (color) as a function of drive power and frequency. This plot is similar to the one in Fig. 13, but here the data were obtained by sweeping power in both directions at a given frequency. Alternate sweep directions are interlaced, allowing one to see the hysteresis in the driven response (striped region in the top left corner). The upper and lower bifurcation boundaries are clearly visible. Inset: reflected signal phase (color) as a function of drive frequency and flux bias for a drive power of −140 dBm. The linear resonant frequency shows the expected periodic dependence on flux bias.

In order to characterize the performance of this device as a flux sensor, we carried out the following experiment. The dc coil was used to bias the SQUID at a sensitive point. The fast flux line was then used to send a small calibrated ac flux signal at a frequency of 10 Hz. A vector network analyzer was used to determine the oscillations in the reflected signal phase, which was then transferred to a computer. These oscillations were then Fourier-transformed and the signal to noise ratio (SNR) of the resulting peak at 10 Hz was determined. Since we know the magnitude of the ac flux signal, we can extract the value of the smallest flux signal, which can be resolved with unity SNR in a 1 Hz bandwidth. We call this number the effective flux noise in our system. Figure 22 shows a plot of the effective flux noise as a function of microwave drive power for three different flux bias points (different sample than one in Fig. 21). One expects the SNR to improve when larger microwave power is used to probe the resonator, resulting in a lower effective flux noise. The dashed lines indicate the improvement expected if the resonator was linear. The advantage of the JBA principle is clearly visible as the nonlinearity sets in at higher drive powers [see Figs. 5(a) and 5(b)]. Under these bias conditions the JBA exhibits significant parametric gain, effectively lowering the system noise temperature, and results in the lowest observed flux noise of 1 $\mu\Phi_0/\sqrt{(\text{Hz})}$ for this device. This demonstrates that a microwave readout of a SQUID can lead to a fast sensitive flux detector.

One should note that it is possible to operate the magnetometer in the digital mode by biasing the oscillator in the bistable region as was done for the qubit readout. In this mode, the magnetometer is essentially a 1-bit flux sampler. However for measuring continuous changes in flux, it is a more cumbersome mode of operation involving pulse preparation and processing and one would prefer the analog mode where only a continuous microwave signal is required. We tested the magnetometer in the digital mode (data not shown) as well and obtained similar effective flux noise performance.

We will conclude this section with some remarks about optimizing the performance of such a magnetometer. As mentioned earlier, the system noise temperature of the amplification chain determines the lowest flux noise for a given set of SQUID parameters. In principle, operating the JBA at high parametric gain points should result in a noise temperature approaching the standard quantum limit. We are presently exploring this possibility. The choice of the quality factor Q of the resonator is another important criterion for optimizing effective flux noise. A higher Q will give you a larger phase shift per unit change in flux but at the cost of reduced bandwidth and possibly lower operating powers, which can even make the effective flux noise worse. As the data suggest, accessing the nonlinearity of the SQUID gives you enhanced performance even for a low Q device. However this also comes at the cost of reduced bandwidth (data not shown) since gain-bandwidth for such systems is fixed. Another parameter that influences the effective flux noise is the drive power, and in principle one can improve the performance by increasing it. In practice there is always a maximum operable limit for a given device due to its finite dynamic range of operation, e.g., entering the bistable regime in the JBA. One could also trade-off nonlinearity for higher operating powers by reducing the coupling of the SQUID (nonlinear device) to the resonator (linear device),[56] but this will predictably decrease the phase shift per unit change in flux. To summarize, quality factor, nonlinearity, operating power, and noise temperature are related to each other in a complex way, and we are presently exploring strategies to optimize for minimum effective flux noise and maximum bandwidth.

VII. CONCLUSIONS

The Josephson Bifurcation Amplifier (JBA) exploits the bifurcation dynamics of the microwave-driven plasma oscillation of a Josephson junction. When biased near the bifurcation point, the driven voltage response varies strongly with the plasma frequency which is modulated by a weak external signal parametrically coupled to the critical current of the junction, thus giving rise to amplification. The Josephson Bifurcation Amplifier is capable of both analog and digital dispersive measurement with variable gain.

We have demonstrated experimentaly the principle and operation of this novel amplifier by observing the Josephson plasma oscillation transition between the two dynamical states predicted for a driven nonlinear system. Using different samples, we have shown that this dynamical phenomenon is stable, reproducible, and can be precisely controlled, thus opening the possibility for practical applications such as amplification. A signal coupled to the critical current of the junction can be detected by monitoring the changes in the dynamical state of the nonlinear oscillator.

This approach was used to develop a nonlinear dispersive readout for superconducting qubits by coupling a Cooper-pair box with the JBA. In order to perform a readout, the resonator is rf-energized to a level where its oscillation state now acts as a sensitive pointer of the qubit state. This technique does not generate any dissipation on-chip since the resonator is only damped by circuitry outside the chip, i.e., a 50 Ω transmission line with a matched circulator and amplifier, and enables a high-fidelity qubit readout with a megahertz repetition rate. We have measured Rabi oscillations and Ramsey fringes with sufficient speed that real time filtering to correct for drifts in the charge and flux bias becomes possible. Also, several successive readouts may be performed within the energy relaxation time of the qubit (T_1). This gives valuable information on the readout-induced interaction between the qubit and its environment and accounts for the observed contrast.

We also exploited the JBA principle to construct a high speed magnetometer. This was done by incorporating a tunnel junction SQUID in a coplanar stripline resonator operating at 1.3 GHz. Using the nonlinearity of the SQUID, we were able to achieve an effective flux noise of about 1 $\mu\Phi_0/\sqrt{\mathrm{Hz}}$. Further improvements are possible by optimizing the flux to critical current transfer function of the SQUID. This method can be extended to high speed magnetometry of single molecule magnets by replacing the tunnel junction SQUIDs with nano-SQUIDs which use nanoconstrictions as the Josephson elements.

The advantage of the JBA over other dissipative amplification techniques such as the dc SQUIDs resides in its minimal back-action. Since there is no on-chip dissipation, the only source of back-action is the matched isolator load, which is efficiently thermalized at the bath temperature. An important point is that in the JBA, only fluctuations from the load that occur in a narrow band centered about the plasma frequency contribute to the back-action, whereas in the dc SQUID noise from many high frequency bands is also significant. Finally, the bifurcation amplifier does not suffer from quasiparticle generation associated with hysteretic SQUIDs (Ref. 57) and dc current-biased junctions[58] which switch into the voltage state. Long quasiparticle recombination times at low temperatures limit the acquisition rate of these devices, while the recombination process itself produces excess noise for adjacent circuitry.[59]

We would like to thank M. Metcalfe, C. Rigetti, E. Boaknin, and V. Manucharyan for their contribution to the JBA and CBA experiments. We would like to acknowledge M. Hatridge for his contribution to the magnetometry experiments. Funding from the following sources is acknowledged: AFOSR under Grant No. FA9550-08-1-0104 (R.V. and I.S.), ONR under Grant No. N00014-07-1-0774 (I.S.), NSA under ARO Contract No. W911NF-05-1-0365, NSF under Grant No. DMR-0653377 (M.H.D.), the Keck Foundation (M.H.D.), the Agence Nationale de la Recherche (M.H.D.) and College de France (M.H.D.).

[1] B. D. Josephson, Rev. Mod. Phys. **36**, 216 (1964).
[2] A. B. Zorin, Phys. Rev. Lett. **76**, 4408 (1996).
[3] R. J. Schoelkopf, P. Wahlgren, A. A. Kozhevnikov, P. Delsing, and D. E. Prober, Science **280**, 1238 (1998).

[4] M. Muck, C. Welzel, and J. Clarke, Appl. Phys. Lett. **82**, 3266 (2003).
[5] A. J. Dahm, A. Denenstein, T. F. Finnegan, D. N. Langenberg, and D. J. Scalapino, Phys. Rev. Lett. **20**, 859 (1968).
[6] T. Holst and J. B. Hansen, Physica B **165**, 1649 (1990).
[7] T. A. Fulton and L. N. Dunkleberger, Phys. Rev. B **9**, 4760 (1974).
[8] E. Il'ichev, T. Wagner, L. Fritzsch, J. Kunert, V. Schultze, T. May, H. E. Hoenig, H. G. Meyer, M. Grajcar, D. Born, W. Krech, M. V. Fistul, and A. M. Zagoskin, Appl. Phys. Lett. **80**, 4184 (2002).
[9] I. Siddiqi, R. Vijay, F. Pierre, C. M. Wilson, M. Metcalfe, C. Rigetti, L. Frunzio, and M. H. Devoret, Phys. Rev. Lett. **93**, 207002 (2004).
[10] A. Lupascu, C. J. M. Verwijs, R. N. Schouten, C. J. P. M. Harmans, and J. E. Mooij, Phys. Rev. Lett. **93**, 177006 (2004).
[11] I. Siddiqi, R. Vijay, F. Pierre, C. M. Wilson, L. Frunzio, M. Metcalfe, C. Rigetti, R. J. Schoelkopf, M. H. Devoret, D. Vion, and D. Esteve, Phys. Rev. Lett. **94**, 027005 (2005).
[12] V. E. Manucharyan, E. Boaknin, M. Metcalfe, R. Vijay, I. Siddiqi, and M. Devoret, Phys. Rev. B **76**, 014524 (2007).
[13] M. Metcalfe, E. Boaknin, V. Manucharyan, R. Vijay, I. Siddiqi, C. Rigetti, L. Frunzio, R. J. Schoelkopf, and M. H. Devoret, Phys. Rev. B **76**, 174516 (2007).
[14] K. Wiesenfeld and B. McNamara, Phys. Rev. Lett. **55**, 13 (1985).
[15] J. S. Aldridge and A. N. Cleland, Phys. Rev. Lett. **94**, 156403 (2005).
[16] V. M. Eguíluz, M. Ospeck, Y. Choe, A. J. Hudspeth, and M. O. Magnasco, Phys. Rev. Lett. **84**, 5232 (2000).
[17] S. Martignoli, J.-J. van der Vyver, A. Kern, Y. Uwate, and R. Stoop, Appl. Phys. Lett. **91**, 064108 (2007).
[18] B. Yurke, L. R. Corruccini, P. G. Kaminsky, L. W. Rupp, A. D. Smith, A. H. Silver, R. W. Simon, and E. A. Whittaker, Phys. Rev. A **39**, 2519 (1989).
[19] R. Movshovich, B. Yurke, P. G. Kaminsky, A. D. Smith, A. H. Silver, R. W. Simon, and M. V. Schneider, Phys. Rev. Lett. **65**, 1419 (1990).
[20] R. Vijay, Ph.D. thesis, Yale University, 2008. Available online at http://qulab.eng.yale.edu/archives.htm.
[21] M. A. Castellanos-Beltran and K. W. Lehnert, Appl. Phys. Lett. **91**, 083509 (2007).
[22] N. Bergeal, R. Vijay, V. E. Manucharyan, I. Siddiqi, R. J. Schoelkopf, S. M. Girvin, M. H. Devoret, arXiv:0805.3452v1
[23] M. Metcalfe, Ph.D. thesis, Yale University, 2008. Available online at http://qulab.eng.yale.edu/archives.htm.
[24] M. I. Dykman and M. A. Krivoglaz, Physica A **104**, 480 (1980).
[25] O. Naaman, J. Aumentado, L. Friedland, J. S. Wurtele, and I. Siddiqi, Phys. Rev. Lett. **101**, 117005 (2008).
[26] A. Wallraff, D. I. Schuster, A. Blais, L. Frunzio, J. Majer, M. H. Devoret, S. M. Girvin, and R. J. Schoelkopf, Phys. Rev. Lett. **95**, 060501 (2005).
[27] M. Hatridge, R. Vijay, J. J. Lee, J. Clarke, and I. Siddiqi (unpublished).
[28] M. I. Dykman, I. B. Schwartz, and M. Shapiro, Phys. Rev. E **72**, 021102 (2005).
[29] D. J. Van Harlingen, T. L. Robertson, B. L. T. Plourde, P. A. Reichardt, T. A. Crane, and J. Clarke, Phys. Rev. B **70**, 064517 (2004).
[30] M. I. Dykman and V. N. Smelyansky, Zh. Eksp. Teor. Fiz. Pis'ma Red. **94**, 61 (1988).
[31] M. Marthaler and M. I. Dykman, Phys. Rev. A **73**, 042108 (2006).
[32] M. I. Dykman, Phys. Rev. E **75**, 011101 (2007).
[33] J. M. Martinis, M. H. Devoret, and J. Clarke, Phys. Rev. B **35**, 4682 (1987).
[34] R. Vijay, I. Siddiqi, P. Hyafil, M. Metcalfe, L. Frunzio, and M. H. Devoret (unpublished).
[35] E. Boaknin, V. E. Manucharyan, S. Fissette, M. Metcalfe, L. Frunzio, R. Vijay, I. Siddiqi, A. Wallraff, R. J. Schoelkopf, and M. Devoret, arXiv:cond-mat/0702445 (2007).
[36] D. F. Santavicca and D. E. Prober, Meas. Sci. Technol. **19**, 087001 (2008).
[37] Y. Nakamura, Y. A. Pashkin, and J. S. Tsai, Nature (London) **398**, 786 (1999).
[38] J. E. Mooij, T. P. Orlando, L. Levitov, L. Tian, C. H. van der Wal, and S. Lloyd, Science **285**, 1036 (1999).
[39] D. Vion, A. Aassime, A. Cottet, P. Joyez, H. Pothier, C. Urbina, D. Esteve, and M. H. Devoret, Science **296**, 886 (2002).
[40] J. M. Martinis, S. Nam, J. Aumentado, and C. Urbina, Phys. Rev. Lett. **89**, 117901 (2002).
[41] J. Koch, T. M. Yu, J. Gambetta, A. A. Houck, D. I. Schuster, J. Majer, A. Blais, M. H. Devoret, S. M. Girvin, and R. J. Schoelkopf, Phys. Rev. A **76**, 042319 (2007).
[42] I. Siddiqi, R. Vijay, M. Metcalfe, E. Boaknin, L. Frunzio, R. J. Schoelkopf, and M. H. Devoret, Phys. Rev. B **73**, 054510 (2006).
[43] A. Lupascu, E. F. C. Driessen, L. Roschier, C. J. P. M. Harmans, and J. E. Mooij, Phys. Rev. Lett. **96**, 127003 (2006).
[44] F. Mallet, F. R. Ong, A. Palacios-Laloy, F. Nguyen, P. Bertet, D. Vion, and D. Esteve, Nat. Phys. **5**, 791 (2009).
[45] F. Wellstood (private communication).
[46] G. Ithier, E. Collin, P. Joyez, P. J. Meeson, D. Vion, D. Esteve, F. Chiarello, A. Shnirman, Y. Makhlin, J. Schriefl, and G. Schön, Phys. Rev. B **72**, 134519 (2005).
[47] N. Boulant, G. Ithier, P. Meeson, F. Nguyen, D. Vion, D. Esteve, I. Siddiqi, R. Vijay, C. Rigetti, F. Pierre, and M. Devoret, Phys. Rev. B **76**, 014525 (2007).
[48] J. A. Schreier, A. A. Houck, J. Koch, D. I. Schuster, B. R. Johnson, J. M. Chow, J. M. Gambetta, J. Majer, L. Frunzio, M. H. Devoret, S. M. Girvin, and R. J. Schoelkopf, Phys. Rev. B **77**, 180502 (2008).
[49] R. W. Simmonds, K. M. Lang, D. A. Hite, S. Nam, D. P. Pappas, and J. M. Martinis, Phys. Rev. Lett. **93**, 077003 (2004).
[50] D. I. Schuster, A. Wallraff, A. Blais, L. Frunzio, R. S. Huang, J. Majer, S. M. Girvin, and R. J. Schoelkopf, Phys. Rev. Lett. **94**, 123602 (2005).
[51] H. Nakano, S. Saito, K. Semba, and H. Takayanagi, Phys. Rev. Lett. **102**, 257003 (2009).
[52] S. D. Bader, Rev. Mod. Phys. **78**, 1 (2006).
[53] D. Drung, J. Beyer, M. Peters, J.-H. Storm, and T. Schurig, IEEE Trans. Appl. Supercond. **19**, 772 (2009).
[54] J. E. Zimmerman, P. Thiene, and J. T. Harding, J. Appl. Phys. **41**, 1572 (1970).
[55] K. K. Likharev, *Dynamics of Josephson Junctions and Circuits* (Gordon and Breach, New York, 1985), Chap. 14, p. 490.
[56] J. A. B. Mates, G. C. Hilton, K. D. Irwin, L. R. Vale, and K. W. Lehnert, Appl. Phys. Lett. **92**, 023514 (2008).
[57] I. Chiorescu, Y. Nakamura, C. J. P. M. Harmans, and J. E. Mooij, Science **299**, 1869 (2003).
[58] A. Cottet, Ph.D. thesis, Université Paris VI, 2002.
[59] J. Mannik and J. E. Lukens, Phys. Rev. Lett. **92**, 057004 (2004).